

2005

Growth mechanism and properties of novel carbon nanocomposite foams

Thomas Edwin Beechem
University of Dayton

Follow this and additional works at: https://ecommons.udayton.edu/graduate_theses

Recommended Citation

Beechem, Thomas Edwin, "Growth mechanism and properties of novel carbon nanocomposite foams" (2005). *Graduate Theses and Dissertations*. 1465.
https://ecommons.udayton.edu/graduate_theses/1465

This Thesis is brought to you for free and open access by the Theses and Dissertations at eCommons. It has been accepted for inclusion in Graduate Theses and Dissertations by an authorized administrator of eCommons. For more information, please contact mschlangen1@udayton.edu, ecommons@udayton.edu.

**Growth Mechanism and Properties of Novel
Carbon Nanocomposite Foams**

Thesis

Submitted to

**The School of Engineering of the
UNIVERSITY OF DAYTON**

**In Partial Fulfillment of the Requirements for
The Degree
Master of Science in Materials Engineering**

by

Thomas Edwin Beechem III

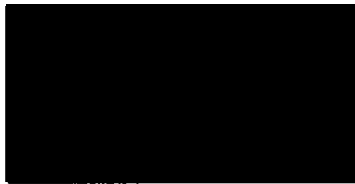
UNIVERSITY OF DAYTON

Dayton, Ohio

May, 2005

GROWTH MECHANISM AND PROPERTIES OF NOVEL CARBON
NANOCOMPOSITE FOAMS

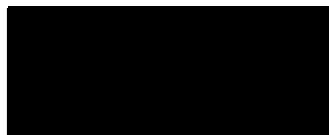
APPROVED BY:



Khalid Lafdi, Ph.D.
Advisory Committee Chairman
Professor, Materials Engineering
Department



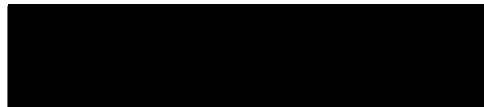
Kevin Hallinan, Ph.D.
Committee Member
Chairperson, Mechanical
and Aerospace Engineering
Department



Lawrence Flach, Ph.D.
Committee Member
Professor, Chemical and Materials
Engineering Department



Donald L. Moon, Ph.D.
Associate Dean
Graduate Engineering Programs
& Research
School of Engineering



Joseph E. Saliba, Ph.D., P.E.
Dean
School of Engineering

ABSTRACT

GROWTH MECHANISM AND PROPERTIES OF NOVEL CARBON NANOCOMPOSITE FOAMS

Name: Beechem III, Thomas, Edwin
University of Dayton

Adviser: Dr. Khalid Lafdi

A testing program was undertaken to further the mechanical properties while simultaneously developing a process property link for mesophase pitch derived carbon foams. First, a novel numerical method was developed predicting the formation of bubbles during foam processing. The model predicts the growth mechanism of a non-spherical bubble assisted for a carbon foam fabrication process. An approach for two dimensional non-spherical mass-diffusion controlled bubble growth in an isothermal Newtonian liquid of infinite extent is considered. Using the two dimensional unsteady form of the equations governing the conservation of mass and momentum, bubble growth is solved as a function of time using a fixed-grid sharp interface finite volume method. A comparative study is performed by considering previous cases of study and shows good agreement, which reflects the

validity of the present model. A parametric study highlighting the effects of the non-spherical growth of the bubble is performed in order to emphasize how controlled bubble growth can be achieved. In each case a change in a particular parameter resulted in a distinct change of the bubble shape.

In addition, a mechanical study of the foams was then embarked upon to investigate the effects of carbon nanofibers on the performance of carbon foams. This study examined the cellular nanocomposites both from a localized and bulk perspective and found that both fiber amount and type play a distinct role in the strengthening of foams as an increase in both was found to cause an associated increase in foam performance. This increase, although lower at the bulk level than at the localized level due to complex loading conditions, is a result both of the strength of the nanofibers themselves as well as the effect the nanofiber has on the molecular arrangement of the graphene layers. Through microscopy analysis, it was found that the addition of nanofibers leads to a ligament morphology similar to that of a standard carbon fiber. It was also determined that the shape of the ligament plays a large role in performance of the foam with increasing aspect ratio leading to increased performance. This knowledge is then used to formulate a theory for a processing scheme resulting in tailored foams with heightened mechanical properties.

List of Figures

Chapter 1 Introduction and Review of Literature

Fig. 1.1 Reticulated (a) vs. Pitch based (b) carbon foams	4
Fig. 1.2 Difference in molecular architecture of synthetically derived pitch (left) and petroleum derived pitch	6
Fig. 1.3 Graphitic arrangement of carbon foam	24

Chapter 3 Numerical Study: Bubble Growth Mechanism in Carbon foams

Fig. 3.1 Estimated specific modulus/property chart of pitch based carbon foams and competing materials	42
Fig. 3.2 Polarized light image showing non-spherical bubbles	43
Fig. 3.3 Illustration of the problem	49
Fig. 3.4 Sample grid	55
Fig. 3.5 Bubble growth vs. time	59
Fig. 3.6 Non-spherical growth vs. time	61
Fig. 3.7 Effect of initial pressure on growth.....	61
Fig. 3.8 Effect of initial bubble press. on non-spherical behavior of bubble	62
Fig. 3.9 Effect of P_{g0} on final bubble size and shape	62
Fig. 3.10 Effect of $d\eta/dt$ on bubble growth rate.....	64
Fig. 3.11 Effect of $d\eta/dt$ on final bubble shape	65
Fig. 3.12 Effect of $d\eta/dt$ on final bubble size and shape	65
Fig. 3.13 Effect of initial bubble radius on growth	67

Fig. 3.14 Effect of R_o on final bubble shape.....	69
Fig. 3.15 Effect of R_o on final bubble size and shape	69

Chapter 4 Carbon Foam Mechanics: Examining...

Fig. 4.1 Structural changes as function of heat-treatment temperature	75
Fig. 4. 2 Disclinations in carbonaceous mesophase.....	76
Fig. 4.3 (a) Low magnification optical micrograph of carbon foam (b) Optical micrograph showing both ligament and node	77
Fig. 4.4 (a & b) Ligaments with disclination	77
Fig 4.5 (a & b) Nodes with disclination	78
Fig 4.6 Bright field image of graphitized foam	79
Fig 4.7 (a & b) 002 dark field and bright field images of ligament relatively free of disclinations (c) selected area diffraction of centered area of ligament free	81
Fig. 4.8 High resolution image of areas on the ligament showing preferential orientation and $-\pi$ wedge disclination.....	82
Fig 4.9 (a) Cross section of pitch based carbon fibers. (b) High resolution imaging of areas of folding and ziga-zag textures (circled area in Fig. 10a)	84
Fig. 4.10 Top view of ligament loading stage	89
Fig. 4.11 Ligament tensile stage.....	90
Fig. 4.12 Bright-field image of pristine carbon nanofibers (PR-24-PS)	93
Fig. 4.13 Effect of shear mixing on foam strength	95
Fig. 4.14 Average specific strength increasing with nanofiber.....	96
Fig. 4.15 Bulk specific strength of foams	97
Fig. 4.16 Bulk specific stiffness of foams.....	98
Fig. 4.17 Ligament strength.....	99

Fig. 4.18 Ligament modulus	99
Fig. 4.19 Ligament strength increases with increasing aspect ratio.....	101
Fig. 4.20 Increasing modulus as aspect ratio increases	101
Fig. 4.21 Normalized ligament strength	102
Fig. 4.22 Normalized ligament modulus	103
Fig. 4.23 Shearing failure characteristic of most ligament fractures	105
Fig. 4.24 a: Pitch based foam with large molecular orientation b: Effect of CNF on molecular orientation	108
Fig 4.25 Granular microstructure of CNF enhanced carbon foams	109

Chapter 5 Bubble Size Distribution of Nanofiber Doped Carbon Foams

Fig. 5.1 Non-uniformity of bubble size in carbon foam.....	113
Fig. 5.2 Increasing average bubble size with temperature	117
Fig. 5.3 Increasing bubble distribution with temperature	117
Fig. 5.4 Increasing average volume size and nanofiber	119
Fig. 5.5 Increasing BSD with nanofiber percentage.....	119

List of Tables

Chapter 1 Introduction and Review of Literature

Table 1.1 Comparison of graphitic crystal structures.....	25
Table 1.2 Comparison of thermal conductivities	30
Table 1.3 Compressive properties of different carbon foams	32
Table 1.4 Tensile properties of different carbon foams.....	32
Table 1.5 Proposed applications for carbon foam	38

Chapter 3 Numerical Simulation: Bubble Growth Mechanism in Carbon Foams

Table 3.1 Physical constants of mesophase pitch used in simulation	53
--	----

Chapter 4 Carbon Foam Mechanics: Examining...

Table 4.1 Characteristics of carbon nanofiber [81]	92
--	----

List of Symbols

- C Concentration of blowing agent in liquid melt
- P_g Pressure inside the bubble
- P_L Pressure of the liquid melt
- P_{g0} Initial pressure inside the bubble
- $P_{L,n}$ Pressure of liquid at the liquid bubble interface
- $P_{v,n}$ Pressure of vapor at the liquid bubble interface
- P_{Lx} X-Component of pressure at computational boundary
- P_{Ly} Y-Component of pressure at computational boundary
- P_a Atmospheric pressure
- R_i Initial bubble radius
- R_x, R_y X and Y coordinates of the bubble radius
- \mathbf{u}_L Vector describing liquid motion in the melt
- U X-velocity of liquid motion in melt
- V Y-velocity of liquid motion in melt
- x_{\max} Last computational point in x domain
- y_{\max} Last computational point in y domain
- K_h Henry's Constant for vapor pressure at gas/liquid interface
- α Factor greater than 1 used as boundary condition insuring non-spherical growth

β Factor greater than 1 used to examine differing initial bubble radii

η Viscosity of liquid melt

σ Surface tension of liquid melt

Pe Peclet number

Re Reynolds number

We Weber number

TABLE OF CONTENTS

Abstract	iii
List of Figures	v
List of Tables	viii
List of Symbols..	ix
Chapter 1 Introduction and Review of Literature	1
1.0 Introduction to topic	1
2.0 Processing of pitch based carbon foams.....	3
2.1 Precursor material	3
2.1.1 Coal derived precursors	4
2.1.2 Petroleum derived precursors	5
2.1.3 Synthetically based precursors.....	7
2.2 Microstructure development methods	7
2.2.1 Thermodynamic flash processing.....	8
2.2.2 Non-thermodynamic flash processing	9
2.3 Post foaming heat treatments.....	10
2.3.1 Stabilization	10
2.3.2 Carbonization	11
2.3.3 Graphitization	11
3.0 Numerical simulation of foaming phenomena.....	12
3.1 Prediction of microstructural arrangement.....	12
3.2 Prediction of bubble growth	14
3.2.1 Nucleation predictions	14
3.2.2 Growth predictions	15
3.2.3 Prediction of mechanical behavior.....	20
4.0 Carbon foam properties	22

4.1	Physical properties	22
4.2	X-Ray diffraction	23
4.3	Thermal properties	26
4.3.1	Graphitic foams	26
4.3.1.1	Effect of precursor on thermal cond.	27
4.3.1.2	Effect of foaming tech. on thermal cond.	28
4.3.1.3	Effect of heat treatment on thermal cond. ..	29
4.3.2	Coefficient of thermal expansion	29
4.4	Mechanical properties	30
5.0	Applications	32
5.1	Current applications	32
5.1.1	Thermal applications	33
5.1.2	Structural applications	34
5.1.3	Internal combustion engine	35
5.1.4	Supercapacitors	35
5.1.5	Solid state reactor	36
5.2	Proposed applications	36
Chapter 2 Purpose of Research		39
Chapter 3 Numerical Study: Bubble Growth Mechanism in Carbon Foams		41
1.0	Introduction	41
2.0	Mathematical definition of the problem	47
2.1	Assumptions.....	48
2.2	Parameters and dimensionless groups	51
2.3	Numerical solution of the governing equations.....	54
2.4	Interface and grid reshaping to solve gov. equations ...	54
2.5	Reshaping the boundary	57
3.0	Results	58

4.0	Conclusions	69
Chapter 4 Carbon Foam Mechanics: Examining...		71
1.0	Introduction	71
1.1	Microstructure of Graphitic Foams (Orientation and Disclination)	74
2.0	Experimental	87
2.1	Acquisition of testing samples	87
2.2	Test method: Bulk Compression	88
2.3	Test method: Ligament Tensile Test	89
3.0	Results	91
3.1	Bulk compression	93
3.2	Ligament tensile tests	98
3.3	Discussion	105
4.0	Conclusions	111
Chapter 5 Bubble size distribution of nanofiber doped carbon foams ...		112
1.0	Introduction	112
2.0	Experimental method.....	114
3.0	Results and discussion.....	116
4.0	Conclusion	121
Chapter 6 The Process Property Link		122
Bibliography		127

Chapter 1

Introduction and Review of Literature

1.0 Introduction to topic

Due to its many forms and wide range of physical characteristics, carbon is utilized in an innumerable amount of applications throughout the world. Running the gamut from structural material and absorbent material to thermal insulator or electrical conduit, carbon has found use in virtually every major industry [13]. This versatility of carbon, when coupled with the weight and surface advantages inherent in a cellular material, has made the study of a novel form of carbon, carbon foam, quite popular.

Carbon foams began to be investigated in earnest in the latter part of the 1960's with the innovation of vitreous carbon foams chiefly by the Union Carbide Company [27]. These foams, with their high thermal stability and low bulk density, were a material of high promise as insulators and construction materials for the aerospace industry in addition to being mentioned for biological applications [92, 69]. This new material was made by coating a rigid urethane foam with a furfuryl alcohol and after initial room temperature curing; the system would be carbonized to create the glassy foam structure [90, 27]. This processing technique, however, proved to

be both complex and time consuming and when coupled with the inability of these foams to be transformed into a wholly graphitic form, innovation soon plateaued [71, 50].

Interest in carbon foams was soon revived in the early 1990's due to the discovery that a carbon fiber precursor, mesophase pitch, could easily be transformed into a new kind of carbon foam capable of being nearly completely graphitizable. This precursor, the main precursor in the making of many graphitic carbon fibers, has the unique ability to form highly aligned graphitic planes during processing, an aspect that aids both the strength and thermal properties of the subsequent product [89,13,68]. In conventional composites, this alignment is exploited through the implementation of a disconnected network of graphite planes, the fiber, connected through a matrix binder to form a material with attractive properties. This disconnected network results in a material whose characteristics are very attractive in the direction of the fibers but poor normal to these fibers. When foamed, this same alignment is achieved, but in addition, the graphitic network is now connected producing attractive isotropic properties [30, 31].

As a result of the connected graphitic network, pitch-based carbon foam has emerged as a material of great promise in a variety of applications. Rocket nozzles, advanced tooling, engine components, and as a core material in sandwich structures have all employed carbon foams due to their attractive thermal and mechanical properties [87,105]. Furthermore, with a

specific modulus rivaling that of a Kevlar honeycomb, carbon foam has even been suggested as a replacement for a vast array of materials ranging from balsa wood and polymer matrices, to metallic honeycombs and titanium for use in biological applications [105]. Due to this wide range of application, research in pitch-based carbon foam has accelerated in the past fifteen years. Yet at the present time there has been no work summarizing the accomplishments thus far in carbon foam research. Consequently, this chapter aims to produce a review of the progress made by those studying carbon foams in an effort to clearly delineate the efforts completed thus far and the labor soon to be undertaken.

This work will focus only on pitch based carbon foams, hereafter referred to as carbon foams, since the vast majority of work being done in the subject is concentrated on this type of foam. The processing of these types of foam will first be examined, followed by a summary of the numerical modeling done in the subject. This work will then offer a synthesis of all properties currently published in the literature followed by a listing of the applications which carbon foam has both been utilized in and suggested for.

2.0 Processing of Pitch Based Carbon Foams

2.1 Precursor Material

Glassy carbons are characterized by their "paracrystalline" structure which is much less ordered than that of graphite as indicated by their density differences of 2.26 g/cm^3 to 1.5 g/cm^3 , respectively [69]. Vitreous carbon foams adopt this glassy form as a result of minimal alignment occurring in the

precursor resins during formation of the foam. Contrarily, in any mesophase pitch-based foam the precursor resin has the ability to become highly aligned during processing due to liquid crystal transformations [29, 68]. The degree to which this alignment occurs will be the key constituent in determining pitch-based carbon foam's physical attributes [68]. Currently, coal, petroleum, and synthetic precursors dominate the manufacturing of carbon foams and as such their differences are delineated below. The more spherical morphology of pitch based carbon foams can be seen in comparison to the more linear reticulated foams in figure 1.1.

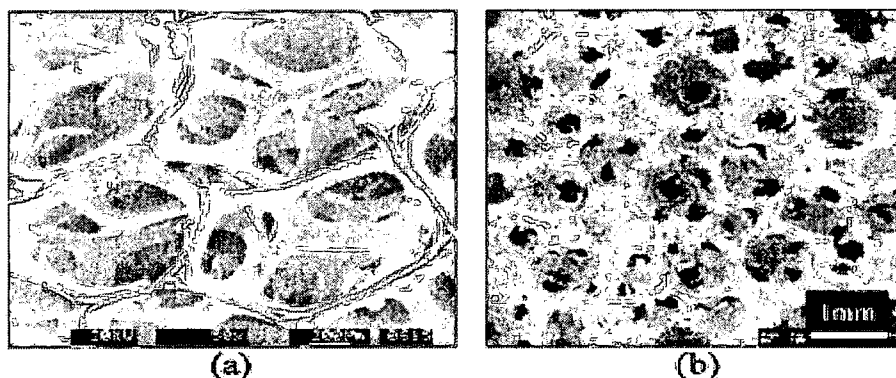


Fig 1.1 Reticulated (a) vs. Pitch-based (b) foams [60]

2.1.1 Coal Derived Precursors

Stiller, Stansberry, and Zondlo working at West Virginia University pioneered the use of coal as a precursor for carbon foams in the late 1990's. Taking a bituminous coal and transforming it into a mesophase pitch, the coal is first hydrogenated using tetralin, where it is then extracted in a manner to remove inorganic species through the use of tetrahydrofuran (THF). The hydrogenated coal is then de-ashed and extracted using a toluene mixture.

The extracted species is an asphaltene, or coal derived pitch precursor [99,101,102]. The resulting precursor has the ability to achieve high alignment of the liquid crystals resulting in a partly graphitizable carbon foam. Stiller et al. then assert that this technique allows for the tailoring of alignment by mixing the hydrogenated and unhydrogenated coals before foaming. Using this technique yields of up to 50% have been reported [99,100,101,102].

The level of graphitization produced using this type of precursor is not published to the best of the author's knowledge. It is stipulated that using this type of precursor results in a foam that can be used as a thermal conductor thus indicating a significant amount of graphitization, however, there are no papers published in which a coal precursor has been examined to quantify its graphitic crystal structure [101,100]. Mechanically, foams being produced through use of a coal precursor have been reported to have specific strengths up to almost 95 MPa [98, 105].

2.1.2 Petroleum Derived Precursors

A petroleum residue is transformed into a mesophase pitch via catalytic modification, hydrogenation, thermal, or solvent modification [13]. Petroleum derived pitches are typically more "disc-like" than their rod-like synthetic counterparts as can be seen in figure 1.2 [50]. This morphology, along with factors such as aromaticity and molecular weight, can significantly affect the viscosity of the pitch during foam processing and result in substantial changes in both the cell size and morphology of the subsequent foam [50, 67]. This

effect is seen as reports of cell sizes being as small as 50 microns using petroleum derived pitches have been reported, a size nearly $1/6^{\text{th}}$ of that of synthetic pitches at identical processing conditions [22].

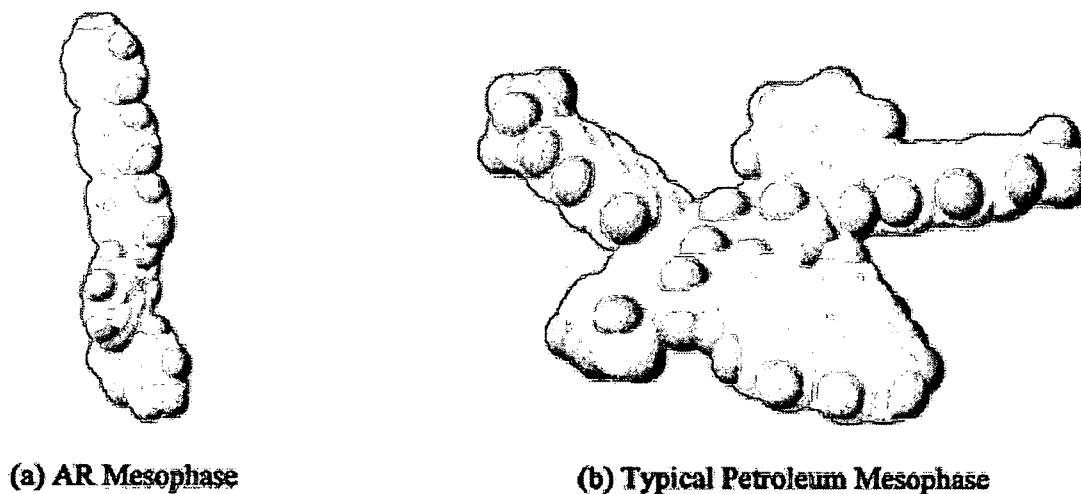


Fig 1.2 Difference in molecular architecture of synthetically derived pitch (left) and petroleum derived pitch [50]

The disc-like nature of the precursor molecule, while affecting cell size, does not inhibit the foam from attaining a highly aligned graphitic state. Examination of petroleum derived foams has found that the degree of graphitization and size of graphitic crystals are comparable even to that of high thermal conductivity carbon fibers [54, 50]. Even with these large graphitic regions, reports on the thermal properties of petroleum-derived foams have indicated lower thermal conductivities than similarly processed synthetic pitches [50]. The reported 15% reduction in thermal diffusivity is believed to be a result of the higher level of initial impurities in petroleum pitches which lead to lattice imperfections. This effect, however, has only been theorized and has not been substantiated experimentally [50].

2.1.3 Synthetic Based Precursors

Using a catalytic modification technique, pitches can be produced synthetically, a process most successfully utilized by the Mitsubishi gas company which produces over 1000 tons a year of synthetic mesophase pitch [13]. This synthetic pitch has a more rod-like mesophase molecule which confers this type of pitch with its low viscosity and softening point [3]. Due to these attractive properties and the ability for these types of molecules to transform into large graphitic sheets, the vast majority of pitch-based carbon foam research has utilized synthetic mesophase pitches [89, 3, 74, 15, 54, 41, 42, 50, 22, 64, 75, 21].

Synthetic pitches have proven to be the most versatile of the carbon foam precursors as they have been utilized in a host of different processing techniques [42, 56]. In each case, they have been easily graphitizable, resulting in thermal conductivities of up to 476 W/m-K [76, 114]. Secondly, mechanical properties of synthetic based precursors have been examined with specific strengths reaching up to 281 MPa [76]. It should be noted that physical properties of foams are as dependent upon the processing as on the precursor.

2.2 Microstructure Development Methods

During foam processing, the precursor is subjected to heat beyond its softening point. After softening, vapor is expelled from the melt through various methods. As this vapor coalesces into bubbles, the liquid surrounding

the bubbles flows in a manner aligning the mesophase molecules in the ligaments separating the bubbles similar to that which occurs during melt spinning of carbon fibers [32,34]. The manner and extent to which these bubbles grow determines the microstructure of the foam and to a large extent the thermal, electrical, and mechanical properties of the subsequent foam. Two major bubble growth techniques have dominated research, thermodynamic flash and non-thermodynamic flash, and are elucidated below.

2.2.1 Thermodynamic Flash Processing

Also known as the Wright Patterson technique from the location of its first implementation, the making of a foam begins by grinding a mesophase pitch into a powder of particle size ranging from 0.5 to 10 microns [42]. The powder is then pressed to an extent that voids are present while the powder is transformed into pellet form. The now pressed pellet is then placed into a pressure vessel where it is pressurized to about 500 psi by an inert gas, usually nitrogen, in order to fill the voids [42]. The pellet is then heated under this pressure to about 10° to 40°C above its softening temperature at which point additional pressure is often applied to obtain a final pressure somewhere between 1000 to 1500 psi [42]. Above its softening temperature, the pitch flows to seal around the inert gas, at which point the pressure is rapidly released causing a thermodynamic flash in the system.

This thermodynamic flash causes the gas trapped by the pitch to rapidly expand forming bubbles and eventually, due to the bursting of these bubbles,

giving the foam its open cell orientation. This rapid growth causes the mesophase molecules to align along the ligaments separating these bubbles, resulting in the foams attractive properties. This growth truncates as the viscosity increases quickly due to the decrease in temperature accompanied by the pressure release.

Several researchers have studied variations of this technique in recent years. For example, in 1999 Anderson et al. reported that through modifications in the final temperature and pressure in the reactor the density of final foam could be tailored to a specific application [4, 14, 15]. Similarly, it has been found that changes in the type of inert gas pressurizing the vessel will result in significant changes in foam microstructure [41]. Finally, viscosity of the liquid melt is known to have a significant role in the formation and growth of bubbles in the system [3].

2.2.2 Non-Thermodynamic Flash Techniques

The technique, a natural derivative of reticulated foam processing, was first pioneered using a pitch precursor in the late 1990's [99]. In this process, the precursor is heated until the coking stage, whereupon, volatiles evolve off of the pitch material and form bubbles thus determining the structure of the foam. Based on this type of method, a higher level of control and tailorability of the microstructure was developed at Oak Ridge National Lab in the late 90's.

The ORNL technique is at the leading edge of non-flash techniques and as a result its details are included here. First, a mold filled with pressed pitch

granules are placed in a reactor which is evacuated to less than 1 Torr [56]. The pitch is then heated to a temperature 50° to 100° C above the pitch's softening point where the vessel's evacuation is released to a nitrogen bath. The system is then pressurized to a level of 1000 psi while the temperature is raised to a point sufficient to coke the pitch [56]. At this point, the pressure and temperature of the system are reduced at a controlled rate to affect the evolution of the volatiles off the system. This evolution of volatiles, along with the rate of temperature and pressure decrease, will determine the size and shape of the bubbles and hence determine the structure of the subsequent foam. Variations in the final temperature as well as rate of pressure release have been reported to have a significant effect on the microstructure of the foam [60].

2.3 Post Foaming Heat Treatments

2.3.1 Stabilization

In the thermodynamic flash technique, the initial foam, which has not been rid of its non-carbonaceous constituents, can be considered as a thermoplastic like material [13]. Consequently, if directly heated to a coking temperature, the material will soften and lose its cellular structure. It is, therefore, necessary in the flash type of processed foam to perform a stabilization step before carbonization of the foam can occur. The stabilization, which effectively crosslinks the material with oxygen, occurs by heating the foam in an air or oxygen atmosphere for several hours at a

temperature of around 200°C until the foam accrues a weight gain of between 5 and 8% [43].

Contrarily in non-flash techniques, there is no need for the stabilization step due to the simultaneous foam formation with coking [56]. Finally, it should also be noted that there has been no published studies regarding the effect which the extent of stabilization has on final foam properties.

2.3.2 Carbonization

Foams are carbonized in order to remove all heteroatoms from the system to achieve a carbon content of over 95%. A turbostratic like structure is formed during this step giving the material a significant increase in mechanical strength [13]. This is achieved by heating the foam to a temperature of about 1000°C where it is held for approximately an hour under in an inert atmosphere [43, 56]. Kearns stipulates that the heating rate must carefully be controlled to be within 1° to 3° C per minute. There is, however, no published works that compare final foam properties to the heating rate of the carbonization stage.

2.3.3 Graphitization

After being carbonized, the foams are then subsequently heated to a temperature between 2000° and 3000° C in order to completely graphitize the system. In this step, mechanical properties increase and the behavior of the material transforms from a thermal and electrical insulator to a conductor [13]. Specifically, foams are typically heated to a temperature between 2400° and

2800° C and held at this temperature for 1 to 10 minutes under an inert blanket [43, 56].

Klett reports that the heating rate during graphitization distinctly affects the crystal structure of the foam [59]. This is expected since the elimination of defects in the crystal structure is both time and temperature dependent. Properties are optimized with a reduction in heating rate during the graphitization step.

3.0 Numerical Simulation of Foaming Phenomena

3.1 Prediction of Microstructural Arrangement

Cellular materials are composed of a series of struts connected together to form a three-dimensional truss structure [31]. The behavior of the foam when subjected to either thermal or mechanical loads is dependent upon the features of the truss architecture. Significant work has been undertaken in an effort to reveal the features of carbon foam's truss structure and then relate this structure to processing variables. Accomplishing this task allows prediction of thermal or mechanical performance as they relate to processing conditions.

Significant progress was made in the late 1980's in the prediction of a cellular material's mechanical properties based upon an analysis of the truss geometry composing a unit cell. First among these notable studies was the work of R.M. Christensen who proposed the structure of cellular material to be composed of a random orientation of struts connected in a manner assuring isotropic behavior [9]. Warren and Kraynik differed with

Christensen's random strut orientation by assuming a series of identical tetrahedral unit cells oriented randomly thus assuring isotropic behavior in their analysis [111]. Ashby and Gibson then used a simpler scheme by assuming a cubic arrangement of square struts with adjacent cells connected at their midpoints with similar results to Warren and Kraynik [25].

During the Material Research Society Symposium Proceedings of 1992, a group from Wright Patterson Research Base led by Joe Hager offered the first substantial effort at predicting the truss architecture of carbon foams [30, 2]. In this body of work, the group first performed a micrographic examination using an SEM of carbon foam in order to delineate the preferred structure of the foams experimentally [2]. The study statistically confirmed and described the basic structure of carbon foams, a structure composed of trigonal ligaments meeting in groups of four at the junctions. Previous studies had either ignored the trigonal nature of the ligaments or placed the unit cells in a non space-filling manner rendering the predictions divergent from the actual material.

As a consequence of these limitations in previous models, Hager reported a structure accounting for these two conditions while predicting a ligament structure based on processing parameters [31]. In this model, these conditions were met by assuming that bubbles nucleate on the lattice points of a body centered cubes resulting in unit cells composed of tetrakaidecahedrons [31]. Tetrakaidecahedron are composed, however, of predominately four and six sided polygons. The parallel micrographic study

indicated in contrast to this assertion that unit cells in carbon foams were composed chiefly of five sided polygons making a series of dodecahedrons [2]. The dodecahedral arrangement when stacked together in a manner to most efficiently take up space was then shown to closely mimic the structure measured micrographically [2]. A year later, Hager and Anderson related this structure to highly idealized processing conditions [29]. This structure is still being employed, most recently being the starting point for a finite element analysis of carbon foams undertaken by Sihn and Roy in 2004 [94].

3.2 Prediction of Bubble Growth

In predicting the microstructural arrangement of carbon foams, several assumptions are made regarding the formation and growth of bubbles during processing. These studies presume a simultaneous commencement of growth at all bubble locations along with equivalent growth rates of all bubbles [31, 94]. Secondly, minimal correlations are made between the magnitudes of these growth rates with the conditions of processing. Consequently, these microstructural relationships offer only a tenuous relationship between processing conditions and the microstructure of the foams. As a result, several efforts have attempted to establish a stronger link between processing and microstructure formation by predicting bubble nucleation and growth through a simulation of the foaming process.

3.2.1 Nucleation Predictions

The extent to which bubbles nucleate during foam processing directly determines both the cell size and the cell size distribution in all foams [70].

Thus relating the extent of nucleation to processing conditions serves as a link between cell morphology and processing techniques. This link was first examined in a study performed by Colton and Suh in the late 1980's [10, 11]. In this work, a polymeric foam's nucleation rate and density was predicted theoretically and then verified experimentally. Colton and Suh assert that bubble nucleation density along with nucleation rate occur at its greatest rate when both heterogeneous and homogeneous nucleation occur simultaneously.

Using the developed model, a connection between processing and nucleation phenomena could be obtained. The work demonstrated the method in which nucleation varied with differing processing conditions and that maximum nucleation density and rate occurred when an additive is placed in a material close to its solubility limit and the material is saturated with high pressure gas [10, 11]. In 1992, Sandhu and Hager then used the relations of this model to predict both the nucleation density of carbon foams during processing [89].

3.2.2 Growth Predictions

Regardless of the foaming method employed, in all phenomena, bubble growth occurs as a result of exchanges in mass, momentum, and other forms of energy between the vapor and liquid phases. In order to predict growth, these exchanges must be accurately quantified in relation to the specific processing conditions. This prediction is tedious as it links the coupled non-linear differential equations describing the transfer of momentum, mass, and diffusion from the liquid to the bubble. Consequently, there have been

several different approaches employed to accurately predict bubble growth. It should be noted that due to their longer and more extensive use, polymeric foams have been the chief topic of these predictions. Yet the phenomena is qualitatively the same regardless of material, and as such the qualitative trends can be applied to carbon foams.

Plesset and Zwick [82], building on the original work in the subject of Rayleigh [86], offer the first substantial attempt for solving bubble growth in an infinite medium by employing an asymptotic solution to boiling phenomena. In boiling phenomena, thermal energy effects are quite substantial and as such the authors are able to solve for growth only by directly computing the vapor pressure of the bubble from the temperature of the melt. This temperature is only computable, however, by limiting the energy equation to the assumption of a thin thermal boundary layer bordering the bubble. Scriven [93] then took the solution a step further by including radial convection in his correlation of bubble pressure from liquid melt temperature but yet the solution still rested on the assumption of a thin thermal boundary layer. This connection of bubble pressure to system conditions serves as the critical assumption of bubble growth models and has a great affect on the outcome and accuracy of the model and hence has continually been modified. Using this method, growth was accurately predicted at the earliest times of growth as being proportional to the square root of time with errors becoming significant at longer times.

The correlation of bubble pressure to system conditions continued to be critical as growth studies evolved from non-viscous boiling phenomenon to growth studies incorporating growth in viscous media where temperature effects were no longer the main influence. This type of phenomenon, the kind prevalent in processing of carbon foams, was first examined in the work of Barlow and Langlois [6] who examined spherical bubble growth in an infinite medium of viscous liquid. Even with the differing conditions concerning the growth media, they used the assumptions employed previously concerning a thin boundary layer in their correlation of bubble pressure to the system. However, instead of using this layer to correlate temperature to pressure, the authors employed a thin layer technique to link the concentration of the vapor phase to the pressure of the bubble via Henry's Law. This association then allowed for an analytical solution to the differential equations of growth. Rosner and Epstein [88] extended this technique by assuming that concentration of the vapor phase follows a specific polynomial profile in the boundary layer to accurately predict growth. This technique proved to be quite popular and was applied by several researchers subsequently through changes in the polynomial to account for different conditions of growth [35, 107]. Again, however, due to the assumption of growth taking place in an infinite pool of liquid melt, growth was only accurately predicted at early times of growth with errors growing significant as the time of simulation lengthened.

Yet in each of these analytical solutions the major assumption of thin boundary layer serves as a crutch for prediction of growth. In this thin

boundary layer, assumptions are needed to associate the bubble pressure to the conditions of growth and consequently the solutions are highly dependent upon this assumption. These inferences create a mushy zone of calculation in the boundary layer that reduces the accuracy and usefulness of each one of the models.

Finite difference models attempt to alleviate the problem of the mushy zone through a numerical approach to growth. Street et al. [103] used the same boundary layer approach as Plesset and Zwick [82] but employed a finite difference solution instead of the analytical solution employed by the latter. This results in a solution that is only directly dependent upon the thin film assumption at the point of interface between the surface and the melt rather than throughout the entire boundary layer as is the case in previous solutions. Arefmanesh et al. [5] then examined the use of the thin boundary layer approach and found that even in finite difference schemes the method still only produces accurate results at the earliest times of growth with disparities becoming more apparent as growth continues. These errors are irretrievable even with the use of higher order polynomials and consequently the authors proposed a method of solving the spherical growth of bubbles without this polynomial through the use of numerically solved potential functions.

Arefmanesh et al. [5] departed from this thin boundary layer technique and obtained very accurate results where growth was assumed to take place in only a finite volume of liquid, where the polynomials are not needed in the

solution, as defined by the thin liquid shell technique of Amon and Denson [1]. Venerus [108] then compared the two techniques of growth in finite and infinite extents of media to summarize and illustrate the advantages of each approach. Ye et al. [120] solved the problem of the boundary assumption by using a novel sharp interface method where all the pertinent information was calculated from a finite difference scheme thus giving the most accurate model to date.

In each of these models, it was shown that several different processing conditions directly affected the bubble growth and as such the microstructure of the foam. Parameters such as bubble pressure, solubility, surface tension, viscosity, and temperature all had distinct effects on bubble growth. Consequently, these studies have served to identify the factors determining the formation of the microstructure in carbon foam. Yet in each of these studies, a material other than mesophase pitch was used to simulate growth. Consequently, only qualitative assumptions can be made with respect to the weight of individual parameters on the final structure of the foams. Work still must be done to directly simulate bubble growth in carbon foams and thus weigh the effect of each one of these processing parameters.

An initial study in this area was begun in 1992 by Sandhu and Hager who derived a mathematical model of a carbon foam process that accounted for both nucleation and growth without proposing a solution to the governing equations [89]. To the best of the author's knowledge no solution to these equations has yet been proffered to the research community. Recently,

Beechem et al. became the first to model carbon foam growth processes asserting viscosity to be the major parameter determining both growth rate and bubble shape [7].

3.2.3 Predictions of Mechanical Behavior

In order to develop a processing property relationship, several studies have examined the ideal behavior of a cellular material under a mechanical load. These studies are accomplished by first defining a unit cell of the material as described in section 3.2.1. Once defined the unit cell is examined under load to determine its deformation processes. These deformation processes then relate the overall mechanical properties of the cellular material to the properties of the bulk material.

Lo performed one of the first types of these studies in the mid-1960's [72]. In this study, Lo relates the unit cell and hence the truss structure of the foam to the packing characteristics of spheres and solves for the deformation using beam theory. The alignment of struts in the truss structure of the foam determines the manner in which the foam deforms. Lo asserts that a bending mode of deformation dominates when the struts are not aligned while stretching is chief mode of deformation when struts are aligned [71]. Equivalent modulus and Poisson ratio is reported to be related to the void content in an inverse linear relationship. Christensen further supports this claim through a similar relationship obtained through assuming random strut orientation and allowing deformation to only occur axially [9].

Contrarily in the work of Gibson and Ashby, deformation is believed to occur in a bending manner due to shear [25]. Through these studies, it was determined that foams do indeed deform according to a bending mechanism and the effective Young's modulus is related to the porosity of the material squared. In Gibson and Ashby's work, however, the truss structure was assumed to trigonal rather than the observed tetrahedral unit that was discussed in 3.2.1. This difference in truss structure was shown to be of diminutive importance as Warren and Kraynik calculated very similar relationships for the effective modulus and Poisson ratio using a tetrahedral unit structure under realistic assumptions of microstructural arrangement [111, 112]. Recognizing this fact, Hall and Hager then asserted that the bulk modulus of the foam is insensitive to local cell geometry allowing them to relate the bulk modulus to the Young's modulus and porosity of the foam [34].

In all of these models, however, the struts were assumed to be both uniform and isotropic. Yet under polarized light microscopy, it is obvious that these assumptions are not valid as ligaments of pitch derived carbon foams show variances across the ligament. Sihn and Roy tackled this problem in a study performed in 2004 [94]. Using a tetrahedral unit cell similar to the one developed by Hager in 1992, Sihn and Roy varied the properties across the ligament and modeled deformation using a finite element analysis. Through this study it was reported again that bending dominates the deformation mechanism and furthermore that effective modulus is most dependent upon the transverse properties of the struts. Consequently, processing schemes

improving this property would most effectively improve carbon foam performance.

4.0 Carbon Foam Properties

4.1 Physical Properties

The physical properties of carbon foams are dependent on the precursor material as well as the processing of that precursor. It has been shown that the degree of porosity in a foam directly determines the physical properties of that foam [9, 111, 25, 94, 20]. Consequently, due to the porosity dependence of the foam, it is erroneous to simply compare the magnitudes of physical properties of two differently processed foams in order judge their effectiveness. Rather, to truly judge a precursor or processing technique, the properties of the separate foams must be compared on a unit weight or specific basis. Therefore, in the proceeding sections, the absolute property values are transformed to a specific nature by using the listed density range in order to offer an accurate comparison of different foaming techniques and precursors.

4.2 X-ray Diffraction

Pitch based carbon foams are of extreme interest because of their ability to be transformed into a highly ordered graphitic structure. As stated previously, thermal and mechanical properties are highly dependent upon the degree of perfection in this graphitic lattice [13, 60]. Consequently, several

studies have attempted to quantify the degree of graphitic perfection possible during the processing of carbon foams.

X-ray powder diffraction analysis is commonly used to probe the graphitic structure of the foam resulting in three key quantifiable properties. These three quantifiable parameters measure the degree of graphitic perfection by measuring: the interlayer spacing (d_{002}), stacking height (l_c), and finally coherence length (l_a) of the basal planes. In pure crystalline form, graphite has been reported to have an interlayer spacing of 0.3354 nm [50, 60]. To optimize the thermal properties of foam, ligaments should conform to this interlayer spacing while maximizing coherence and stacking height thus insuring a large crystalline graphitic region. In obtaining large crystalline regions, energy flow will be maximized and hence so too will the thermal conductivity and diffusivity [50, 60, 78].

The first comprehensive study on the graphitic arrangement of carbon foams occurred in 2000 in a work by Klett et al. where both synthetically and petroleum derived foams were examined after being processed using ORNL's non-flash technique [50]. Both petroleum and synthetically derived foams were reported to have interlayer separations extremely similar to that of a crystal of graphite, 0.3360 and 0.3355 nm, respectively, values that were supported a year later in a thesis by Morgan and again in 2004 by Klett et al. [50, 60, 78]. Secondly, Klett reports that the spacing and density are inversely related although further experimentation is needed to verify this assertion [50]. These interlayer values were supported once again in 2003

when the spacing was reported to be 0.3363 nm using a synthetically derived foam processed via the flash technique [75]. The larger value in this case is not explained in the literature as flash technique foams have rarely been examined from an x-ray perspective. Nonetheless, in all of these studies, carbon foam's interlayer spacing has been reported to be similar to that of even the highest performance carbon fibers, a fact that can be seen in Table 1.1.

Coherence length and stacking height have also been reported to be comparable to that of high performance fibers. This is seen as both synthetically and petroleum derived pitches using both flash and non-flash processing schemes have reported coherence lengths of up to 20 nm. In much the same way stacking heights have been reported to be as great as 80 nm and while being reported to increase with density, a fact due to the ligaments thickening in denser foams [59, 75, 50]. Due to this degree of crystallinity, up to 98.8 % graphitic as seen in figure 1.3, it is believed that the thermal performance of ligaments in carbon foams is equal or greater to that of even the highest performing carbon fibers [50, 80].

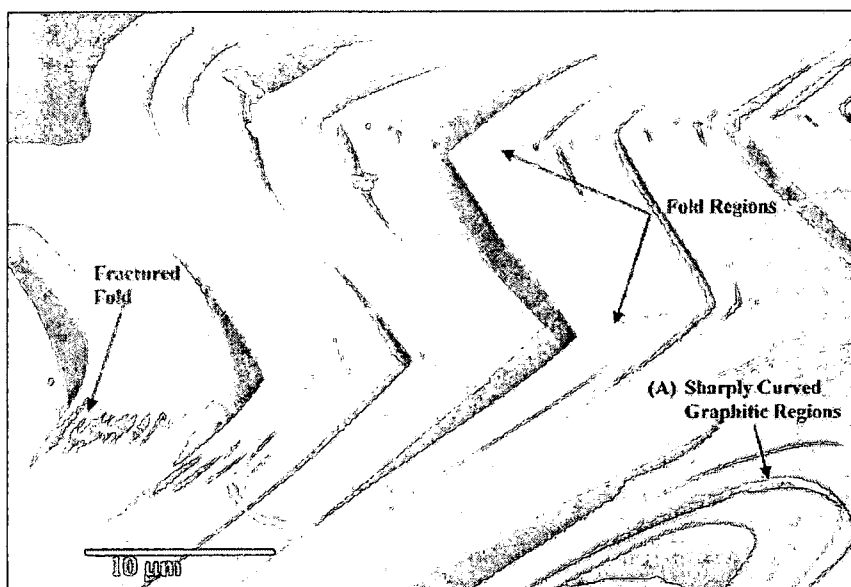


Fig 1.3 Graphitic arrangement of carbon foam [60]

Table 1.1 Comparison of graphitic crystal structures

Graphitic Foam	Type	Density	Interlayer Spacing d_{002}	Stacking Height l_c	Crystalline Size l_a	Sources
ORNL	Regular Processing		0.3358 - 0.3368	44.6 - 442	29	[50,54,55,59,60,76]
Thermodynamic Flash	Regular Processing	0.14 - 0.25	0.3361		20 nm	[60]
West Virginia	Regular Processing	0.048 - 0.8				[98]
Fibers	E35 (67)	2.2	0.3464	3.2	7.2	[60]
	E75 (67)	2.2	0.3421	10.7	22.4	[60]
	E120 (67)	2.2	0.3409	18.9	51.4	[60]
	E130 (67)	2.2	0.338	24	180	[60]
	K1100 fiber (52)	2.2	0.3366	51	85	[60]

4.3 Thermal Properties

A wide range of thermal property values have been reported for carbon foams due to a broad spectrum of precursor, processing, and heat treatment techniques. These differing techniques allow carbon foams to be utilized in applications ranging from thermally insulative to conductive in nature [98]. Post foaming heat treatment greatly determines in what sense carbon foams will be utilized. Foams which are only processed through the carbonization heat treatment, hereafter referred to in this section as carbonized foams, do not have high crystalline order and hence act as insulators. This fact when coupled with a large heat capacity of 0.718 J/g K makes carbonized foams ideal for many applications [78]. Yet there has been little study to the effect of processing conditions, precursors, and heat treatments on carbonized foams.

In contrast to their carbonized counterparts, foams develop high order during the graphitization heat treatment thus giving them a highly conductive structure suitable for many demanding applications [13]. The majority of studies in carbon foam have centered on this type of structure.

4.3.1 Graphitic Foams

During foam processing, liquid crystal regions of mesophase pitch become aligned due to the forces present during bubble expansion [29]. This alignment attained during processing allows for the formation of highly pristine graphitic crystal regions as reported in section 4.2. No better arrangement of graphitic regions is found than in the ligaments of the foam. Consequently, the ligaments of graphitized foams have been reported to have thermal

conductivities in the range of 700-1200 W/m-K while the ligament walls themselves have been estimated to attain conductivities of as much as 1500 W/m-K [91,52]. These values compare extremely well with metals, as copper's thermal conductivity is only 400 W/m-K, however, improvement is still possible and needed as the theoretical conductivity of graphite is over 2000 W/m-K at room temperature [60, 55]. It should be noted that thermal performance of graphite and hence foam can be reduced by up to 40% at high temperatures [20].

In contrast to the high alignment of ligaments, the junctions of the foams are composed of folded graphite layers reducing the thermal conductivity in this region [60,50]. The lower conductivity in the junctions, a fact which is accepted although not quantified in literature, along with the cellular nature results in the bulk foam's typical thermal conductivity to be in the range of 150-200 W/m-K as can be seen in Table 1.2. This value is extremely attractive when examined on a unit weight basis, as the specific thermal conductivities of foam's are 5 times that of aluminum and 6 times that of copper [20, 84, 50, 52, 91, 51]. Due to these high specific properties, several studies have been performed to further elucidate the heat transfer mechanisms in carbon foams in order that foaming precursors, processes, and heat treatments might be optimized.

4.3.1.1 Effect of Precursor on Thermal Conductivity

Using thermodynamic flash as well as non-flash techniques, specific conductivities have been reported to reach up to 460 W/m-K for synthetically

derived foams while in comparison petroleum derived pitches have been reported to reach only 240 W/m-K [22, 114, 50, 76, 84]. Moreover, coal derived pitches have reported even lower specific conductivities in the range of 2.5-97 W/m-K [98, 23, 105]. It should be noted, however, that under the same processing conditions petroleum derived precursors typically perform only 15% less than their synthetic counterparts, a fact that has been reported to be due to a higher impurity content in the petroleum derived pitches [50]. As a consequence of its attractive results and higher availability, most studies have focused on synthetically derived pitches [89, 3, 74, 15, 54, 41, 42, 50, 22, 64, 75, 21].

4.3.1.2 Effect of Foaming Technique on Thermal Conductivity

There are three major foaming techniques which are described in section 2.2. In each case, the method of foaming employed has a distinct effect on the thermal properties of the subsequent foam. In 2000 Oak Ridge National Labs reported over a 70% increase in thermal performance of their foams when their optimized pressure and temperature controlled method was used instead of a straight coking non-flash thermodynamic process [50]. However, the highest performing MER produced foams, a type of foam produced using a flash technique, have outperformed POCO foams, a non-flash foam, by nearly 30% [23].

To the best of the author's knowledge, there has been no reported explanation for this gross property divergence in differing foaming schemes

although it has been reported that foaming rate has a distinct effect on final thermal properties [59]. It should be noted that while both types of processing schemes report to have foams that are completely isotropic, in 2004 Klett contrasted these assertions by reporting that in non-flash techniques the direction of foaming is 3 times more conductive than the other directions [59, 84, 76].

4.3.2 Effect of Post-Foaming Heat Treatment on Thermal Conductivity

The degree of ordering in the graphite planes during heat treatment is both time and temperature dependent. As dwell time at high temperature is increased so too is the amount of order in the foam. As a result, crystal sizes grow and with their growth thermal conductivity increases. This effect has been clearly demonstrated as it has been reported that lowering the heating rate from 10°C/min to 4°C/min results in nearly a 25% increase in the thermal performance of the carbon foam [59].

4.3.3 Coefficient of Thermal Expansion

The coefficient of thermal expansion is critical in applications where two dissimilar materials must be fixed to one another. Carbon foam has the attractive property of an extremely small CTE, 2-3 ppm/°C, whereas most other thermal management metals typically have a CTE between 17-23 ppm/°C [24,20, 80]. This factor makes carbon foam extremely attractive for use with silicon in electronics. No significant changes in the CTE have been reported due to changes in processing schemes or precursor material.

Table 1.2 Comparison of thermal conductivity

Graphitic Foam	Type	Density	Thermal Conductivity	Specific Thermal Conductivity	Sources
ORNL	Isotropic	0.2 - 0.65 g/cm ³	40 - 190 W/mK	148 - 300 (W/mK)	[22,23,50,51,54,55,60,80]
	Anisotropic	0.45 - 0.61 g/cm ³	z125 - 182 W/mK xy41 - 65 W/mK	z277.8 - 331.1 xy91.1 - 106.6 (W/mK)	[60]
Thermodynamic Flash	Regular Processing	0.016 - 0.62 g/cm ³	0.05 - 210 W/mK	0.63 - 484.2 (W/mK)	[23,113]
West Virginia Fibers	Regular Processing	0.16 - 0.5 g/cm ³	0.4 - 17.5 W/mK	2.5 -97 (W/mK)	[23, 98]
	E35 (67)	2.2 g/cm ³	37 W/mK	16.8 (W/mK)	[60]
	E75 (67)	2.2 g/cm ³	110 W/mK	50.0 (W/mK)	[60]
	E120 (67)	2.2 g/cm ³	265 W/mK	120.5 (W/mK)	[60]
	E130 (67)	2.2 g/cm ³	525 W/mK	238.6 (W/mK)	[60]
	K1100 fiber (52)	2.2 g/cm ³	1100 W/mK	500.0 (W/mK)	[60]

4.4 Mechanical Properties

Mechanically, foams have predominantly been examined from a numeric standpoint as is delineated in section 3.2.3. Chiefly through the work of Gibson and Ashby, along with the contributions of Sihm and Roy, it has been clearly stated that carbon foam fails in a bending mode with the magnitude of its strength and modulus directly related to density [25, 94]. Experimentally

little work has been done to understand the failure mechanisms in carbon foams. The effect of precursor, processing, and heat treatment on the strengths of carbon foams can be seen in Table 1.3. It should also be noted that the vast majority of studies have centered on compression properties of foams rather than tensile properties.

The work that has been done to address the mechanical properties of carbon foams has centered on methods to densify the foam in order to increase strength. Infiltration with a polymer or other structural material increases strength at the expense of added weight. In one study, a carbon foam was infiltrated with polyurethane with fourfold increase in specific compressive strength of the foam along with the ability to use the polyurethane at a higher operating temperature due to the superb thermal properties of the foam [8,57].

Foam properties have also been reported to increase when densified using carbon through a chemical vapor infiltration method. Using this method, the specific strength of the carbon foam after densification was shown to increase in much the same magnitude as when infiltrated with polyurethane [54]. Strength is believed to increase due to the mending of cracks and layer separations which are present in the foam due to thermal stress effects of the foaming process [20, 45]. No study has been undertaken to discover the optimal amount of chemical vapor infiltration to maximize the specific properties of the foam.

Table 1.3 Compressive properties of different carbon foams

	Type	Density (g/cm ³)	Compressive Strength (Mpa)	Specific Compressive Strength (Mpa)
ORNL	Regular processing [22, 80, 82]	0.2 - 0.65	1-3.5	3.6-6
	Densification CVD [54]	0.77	31.6	17.7
	Infiltrate with Epoxy [54]	1.3	34.6	26.4
	Poco Foam [80]	0.55	3	5.5
Thermodynamic Flash	Regular processing [8,24,114]	.016-.62	0.08 - 25	1.59-59.52
	Infiltrate with Polyurethane [8]	1.14-1.21	39-46	33.9-34.2
	MER Foam [76]	.016-.62	1.7-7.0	up to 281
West Virginia	Regular processing [23,98,105]	0.048 - 0.8	1.4-41	12.5-95
	Touchstone Cfoam [105]	.16-.50	15.2 to 20.7	Up to 95

Table 1.4 Tensile properties of different carbon foams

	Density (g/cm ³)	Tensile Strength (MPa)	Specific Tensile Strength (MPa)
ORNL [23,79]	0.2 - 0.65	0.7 - 1.6	2.8 - 2.46
Flash Technique [4]	0.12-0.8	0.863-65.3	7.2-81.6
MER [76]	0.016 - 0.62	0.5 - 0.7	2.0 - 2.06
Touchstone Cfoam [105]	0.16 - 0.5	1.14 - 7	5.0 - 14.0

5.0 Applications

5.1 Current Applications

Utilizing the advantages inherent both in cellular and carbonaceous materials, carbon foam is a material of great promise due to a litany of

attractive properties. Among these attractive properties, include the tailorability of its density and porosity, in addition to its intrinsically high specific surface area [24, 42, 56, 40] . Furthermore, foams are attractive as well due to their ease of manufacturing into complex shapes and machinability [24, 105, 61, 64].

Moreover, the chemical nature of carbon gives carbon foams a host of additional attractive aspects, namely, moisture insensitivity, low coefficient of thermal expansion, chemical inertness, high resistance to combustion, and thermal stability up 3000°C in vacuum or 540°C in air, values which can be increased with oxidation protection [98, 8, 105, 62]. Due to these reasons, carbon foam is currently being utilized in several different demanding applications.

5.1.1 Thermal Management Applications

Due to their high thermal conductivity, as delineated in section 4.3, carbon foams have been utilized in many thermally demanding environments, the most popular of which have been in the form of heat exchangers and sinks [44, 55, 63]. Capitalizing on the cellular nature of the foam, one such heat sink design has obviated the need for an active cooling system in electronics due to the system's effective heat transfer coefficient increasing over 40 times with use of a foam over that of traditional materials [55, 58]. This same capability has been capitalized upon in a separate project which has utilized carbon foam as the evaporator in a thermosyphon [12]. Yet in both cases,

the foam has allowed for a design that was drastically smaller than that which was made using traditional materials.

In more demanding environments, an active cooling system has been used in conjunction with carbon foam with both promising thermal and weight saving results. In one such case, a graphitic foam heat sink with forced air flowing through it was used to cool a high performance Pentium 133 microprocessor. In this study, the foam outperformed the standard aluminum material typically employed while weighing 5.5 times less. Furthermore, the foam design was modified to further decrease weight by machining off the fins with performance dropping slightly but with a weight decrease to 11 times less than that of aluminum [24]. Finally, active systems with foam and water as the cooling agent have been able to cool chips at power densities of up to $120\text{W}/\text{cm}^2$ although a significant pressure difference is needed for proper functioning of the system [24, 66].

5.1.2 Structural Applications

Due to a specific modulus rivaling that of a Kevlar honeycomb along with its attractive thermal characteristics [105], carbon foam has been suggested for a variety of structural applications. Sandwich structures are composed of a thermally resistant material coupled with a structural material. Typically the thermally resistant material has little structural value, however, this is not the case with carbon foam implementation [65]. This structural value is seen more clearly as carbon foam has been attached to panels and been used with successful results as a replacement for many metallic honeycombs [65, 66,

80, 50]. Finally, when a fully graphitized foam is placed in between panels, a variety of applications have been shown to be completely plausible ranging from heat pipes to radiators in automobiles saving weight and increasing performance in each case [65, 28,53].

5.1.3 Internal Combustion Engines

Weight, durability, and creep resistance are the critical design parameters for the pistons of internal combustion engines. Aluminum has long been used as it whisks away the heat of the engine chamber, yet these metallic pistons are heavy thus reducing the efficiency of the engine. Consequently, many designs have sought to decrease the weight by combining an aluminum foam with a polymer of high temperature resistance. This has proven problematic, however, as the low thermal conductivity of the piston has led to premature thermal degradation of the engine. Contrarily, using a thermally conductive carbon foam filled with aluminum has solved both problems with a 40% weight reduction providing an engine with higher efficiency and power output [54, 114].

5.1.4 Supercapacitors

High pulse power delivery is needed for many processes in the electronics industry yet with traditional materials battery sizes must increase substantially with this increased performance. Supercapacitors, however, can produce these high pulses resulting in a package which is smaller in size with the advantages of extended battery life and non-degrading stable charge and discharge cycles. Currently, Cooper Electronic Technologies is constructing

supercapacitors from carbon foam calling their product, the PowerStor Areogel capacitor. This capacitor uses an electrochemical double layer arrangement which utilizes carbon foam electrodes with ultrafine pore size in an electrolyte fill environment. The maximum operating voltage is 2.75 volts with a 5.5 volt version currently being developed [17].

5.1.5 Solid State Reactor

Small nuclear reactors have been proposed as the ideal power source for energy generation in the most remote of environments. In a project funded by the DOE's Demand-Driven Nuclear Energizer Module Project, a solid-state nuclear reactor was designed and fabricated with carbon foam as an integral component. Utilizing the strength, heat conduction, and high operating temperature much of the core was composed of carbon foam with promising results [49].

5.2 Proposed Applications

Due to its attractive properties carbon foam has been suggested for a myriad of different applications. In this section, many of these proposed applications that are looming on the horizon will be illuminated in order to expose where the next generation of carbon foams will be utilized.

Due to its high specific properties, carbon foam is ideal for utilization in the field of aeronautics where all designs are constrained by volume and weight considerations. Consequently, carbonized foam has been suggested for use in leading edges of high performance aircraft, rocket nozzles, and as aircraft brakes [40, 105, 79].

Structurally, due to its isotropic properties, carbon foam has been suggested as a replacement for metallic honeycombs and as a core material for interior panels, sandwich structures, non-structural bulkheads, sound absorption panels, as well as a shield for electromagnetic radiation [98, 40, 52, 60, 8, 118, 45, 46, 48]. Using foam as a core material has even been suggested for the support of spaceborne mirrors due to a variety of reasons including its ability to cushion large amounts of kinetic energy [8, 98, 113]. Similarly, from a thermal absorption standpoint, carbon foam infiltrated with a phase change material is believed to find application in the space program as well in the near future [47]. Additional proposed applications can be found in Table 1.5.

Table 1.5 Proposed applications for carbon foam

Aerospace & Defense		Commercial	
Optical benches and lightweight	Composite tooling ¹⁰⁵	Heat exchangers ¹¹⁶	Truck brake ^{114,116}
Thruster nozzles ¹⁰⁵	Abrasive tools ¹⁰⁵	High temp tooling ^{114,116}	High speed train brake ¹¹⁶
Thermal protection systems ¹⁰³	Energy absorbing crash barriers ¹⁰⁵	Acoustic Insulation ^{114,116}	Piston ^{114,116}
Heat transfer systems ¹⁰⁵	Brake disks ^{8,105}	Thermal panel ¹¹³	Battery electrode ¹¹⁶
Light weight antennas ¹⁰⁵	Automobile crush zone capsules ¹⁰³	EMI shielding ¹¹⁶	Multi-layer PWBS ¹¹⁶
Joiner bulkheads ¹⁰⁵	Engine components ¹¹⁶	Ballistic containment cases ¹¹⁶	Multi-chip modules ¹¹⁶
Jet blast deflectors ¹⁰⁵	Catalytic converters ¹⁰⁵	Electronic heat sinks ¹¹⁶	Chip carriers and chip on board ¹¹⁶
Stealthy materials ^{80, 105}	Heat exchangers ¹⁰⁵	Friction/brake ¹¹⁶	Recreational equipment i.e. canoes ¹¹⁶
Lightweight armor ¹⁰⁵	Structural insulated panels ¹⁰³	Leadings edges ¹¹⁶	Clutches ⁸
Ship bulkheads ⁸⁰	High temperature insulation ¹⁰³	Core attachment ¹¹⁶	Fuel cell catalyst support ⁹²
Blast deflectors ⁸⁰	Composite tooling ¹⁰⁵	Heat exchangers ¹¹⁶	Fuel cell electrodes ¹⁰⁵
Armor ⁸⁰			
Thruster nozzles ⁸⁰			

Chapter 2

Research Purpose

Processing of carbon foam is highly complex as it links the transactions between momentum, mass, and energy between a molten precursor and a gas phase. Due to this complexity, the process property link for the material has constantly been reviewed and revised by many researchers since the heavy research of pitch based carbon foams began nearly 15 years ago [2, 29,30,47]. This work serves as another step in establishing a true link between the processing and performance of carbon foams.

Taking this step infers that the processing of carbon foams is suitably understood and predictable. As stated before, due to the complexity of the process and the high rates of transfer between various entities, processing is not thoroughly understood. Consequently, an analytical study investigates the phenomenon of bubble growth during carbon foam processing to better quantify the manner in which microstructure formation occurs. In addition, a physical examination of the microstructure will be undertaken to again gather the effects of processing parameters on the bubble size and uniformity.

With the microstructure thoroughly examined, performance can then be measured. Due to its high thermal capabilities, the majority of carbon foam research has focused on the heat transfer performance of foams. Consequently, the mechanical behavior of foams has not been thoroughly investigated nor understood. This work, consequently, investigates the mechanical performance of carbon foams both from a bulk and localized perspective. In this analysis, the validity of previous models focusing on prediction of foam strengths will be questioned and judged based on their conformation to experimental results. In this mechanical analysis, the effect of nanofibers on the mechanical performance of the cellular material will be quantified as well. The effect of nanofibers will give a first glimpse into the behavior of a cellular nanocomposite both from a performance and processing point of view.

From these dual points of analysis, numerical and mechanical, the next step in linking process and properties of carbon foams will be initiated. This link will then serve as the preparatory steps to the mechanical maximization of mesophase pitch derived foam materials.

Chapter 3

Numerical Study: Bubble Growth Mechanism in Carbon Foams

(Author's Note: This portion of the study has been previously published, Carbon 43(5): 1055-1064. In order that the study presented here not be confused as different from the published article it is displayed here identically as it was published.)

1.0 Introduction

Carbon foam has emerged as a material of great promise in a variety of applications. Rocket nozzles, advanced tooling, engine components, and as a core material in sandwich structures have all employed carbon foams due to their high thermal conductivity and optimum mechanical properties [87,105]. Furthermore with a specific modulus rivaling that of a Kevlar honeycomb, carbon foam has even been suggested as a replacement for a vast array of materials ranging from balsa wood and polymer matrices to metallic honeycombs and titanium for use in biological applications [105]. With this myriad of applications and the potential it shows with respect to other materials as is seen in figure 3.1, it is believed that carbon foam will be utilized with a much increased magnitude in the near future.

An examination of the literature revealed several methods of estimating the mechanical properties of the material [112,9,26,113]. These methods based on graphitic foam ligaments having properties similar to the P-100 carbon fibers and a porosity of 90%, show the potential for a material of lighter weight and higher stiffness[33,34].

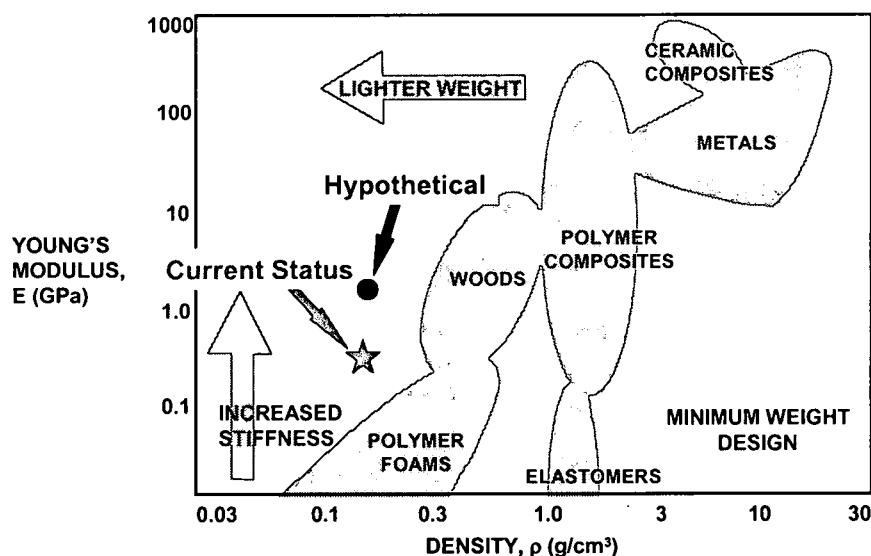


Fig. 3.1 Estimated specific modulus/property chart of pitch-based carbon foam and competing materials [33,34]

The models, which by incorporating finite element meshes and taking into account property variations from the nodes through the center of the struts as well as the anisotropic behavior of the material properties, have shown that the transverse properties in the center of the struts have the most effect on the overall foam mechanical properties [94,95].

Modeling of carbon foam strength characteristics is highly dependent however on the idealized structure which is chosen for the model. In each model mentioned, the structure was assumed as an open network of triangular struts arranged to form pentagons which fit together to form a

dodecahedra or tetrahedral [31,2,29]. This type of structure assumes completely spherical bubbles, an assertion which is not correct, as can be seen in figure 3.2, in the majority of foaming operations. Furthermore, in actual foaming operations to the best of the authors knowledge, there has been no work examining this non-spherical behavior, a behavior which could be exploited to control the anisotropy of the material. Consequently, there is a need for an understanding of the mechanisms that determine non-spherical bubble growth in foams in order for the full potential of the material to be achieved both from a theoretical and processing reference point.



Fig. 3.2 Polarized light image displaying non-spherical bubbles

Carbon foam is typically produced by a sudden release of pressure in a supersaturated solution of gas in a molten precursor [94]. With the release of pressure, bubbles form in the melt and begin to grow due to exchanges of mass, momentum, and energy between the melt and this new vapor phase. This growth determines the microstructure, and as such, the thermal, mechanical, and electrical properties of the subsequent foam. Thus, in order to tailor the properties of the foam, a controlled growth of the vapor phase and

its solubility must be achieved. A complete understanding of the bubble growth mechanism in foam, however, is challenging, and consequently our first study is focused on a numerical computation.

As such there has been extensive work on modeling of the bubble growth in liquids. Modeling the phenomenon is both important and tedious as it links the coupled non-linear differential equations describing the transfer of momentum, mass, and diffusion from the liquid to the bubble. Due to the demanding nature of the problem, there have been several different approaches employed to best model the growth.

Plesset and Zwick [82], building on the original work in the subject of Rayleigh [86], offer the first substantial attempt for solving bubble growth in an infinite medium by employing an asymptotic solution to boiling phenomena. In boiling phenomena, thermal energy effects are quite substantial and as such the authors are able to solve the equation of motion only by directly computing the vapor pressure of the bubble from the temperature of the melt and then solving for growth. This temperature is only computable, however, by limiting the energy equation to the assumption of a thin thermal boundary layer bordering the bubble. Scriven [93] then took the solution a step further by including radial convection in his correlation of bubble pressure from liquid melt temperature but yet the solution still rested on the assumption of a thin thermal boundary layer. This connection of bubble pressure to system conditions serves as the critical assumption of bubble growth models and has

a great affect on the outcome and accuracy of the model and hence has continually been modified.

Consequently, the correlation continued to be critical as growth studies evolved from non-viscous boiling phenomenon to growth studies incorporating growth in viscous media where temperature effects were no longer the only driving force. This type of phenomenon, the kind that is examined in this paper, was first examined in the work of Barlow and Langlois [6] who examined spherical bubble growth in an infinite medium of viscous liquid. Even with the differing conditions concerning the growth media, they used the assumptions employed previously concerning a thin boundary layer in their correlation of pressure to the system. However, instead of using this layer to correlate temperature to pressure, the authors employed a thin layer technique to link the concentration of the vapor phase to the pressure of the bubble via Henry's Law. This association then allowed for an analytical solution to the integro-differential equations of growth. Rosner and Epstein [88] then extended this technique by assuming that concentration of the vapor phase follows a specific polynomial profile in the boundary layer and that this polynomial accurately predicted growth. This technique proved to be quite popular and was applied by several researchers subsequently through changes in the polynomial to account for different conditions of growth [35,106].

Yet in each of these analytical solutions the major assumption of thin boundary layer serves as a crutch for prediction of growth. In this thin

boundary layer, assumptions are needed to associate the bubble pressure to the conditions of growth and consequently the solutions are highly dependent upon the assumptions. These inferences create a mushy zone of calculation in the boundary layer that reduces the accuracy and usefulness of each one of the models.

Finite difference models attempt to alleviate the problem of the mushy zone through a numerical approach to growth. Street et al. [102] used the same boundary layer approach as Plesset and Zwick [82] but employed a finite difference solution instead of the analytical solution employed by the latter. This results in a solution that is only directly dependent upon the thin film assumption at the point of interface between the surface and the melt rather than throughout the entire boundary layer as is the case in previous solutions. Arefmanesh et al. [5] then examined the use of the thin boundary layer approach and found it produces accurate results at the earliest times of growth with disparities becoming more apparent as growth continues. These errors are irretrievable even with the use of higher order polynomials and consequently the authors proposed a method of solving the spherical growth of bubbles without this polynomial through the use of numerically solved potential functions. Arefmanesh et al. [5] obtained very accurate results where growth was assumed to take place in only a finite volume of liquid, where the polynomials are not needed in the solution, as defined by the thin liquid shell technique of Amon and Denson [1]. Venerus [107] then compared the two techniques of growth in finite and infinite extents of media to summarize and

illustrate the advantages of each approach. Ye et al. [119] solved the problem of the boundary assumption by using a novel sharp interface method where all the pertinent information was calculated from a finite difference scheme thus giving the most accurate model to date.

With the help of modern numerical techniques, the problems of the thin boundary layer assumption have been made largely obsolete with the use of, among others, the sharp interface method, yet one glaring weakness of bubble growth studies still remains. Growth is almost always limited to the case of spherical axisymmetric growth. In fact, the vast majority of papers presented on bubble growth have been limited to the assumption of spherical growth. This assumption breaks down, however, in the majority of foaming processes where growth takes place under a non-symmetric pressure gradient.

The focus of this work is to take into account this non-symmetric behavior by solving the diffusional growth behavior of a vapor bubble in a polymeric melt of infinite extent. This will be accomplished by numerical solution of the two dimensional equations for mass, motion, and diffusion through the melt with no assumptions regarding either the concentration or pressure in the system.

2.0 Mathematical definition of the problem

Although a change in shape is permitted in the model of growth, the forces controlling the system are still the same. Surface tension, viscous forces, and liquid inertia each act to retard the growth of the bubble initiated by a pressure

difference across the interface between vapor and liquid. In addition to these forces, diffusion through the liquid to the bubble affects this pressure difference as well. With this explanation, it follows then that the equations of mass, momentum, and diffusion through the liquid define the system.

2.1 Assumptions

The system, rudimentarily illustrated in Figure 3.3, will further be defined by the following assumptions:

1. Bubble growth takes place in the xy plane and is assumed to be symmetric about the vertical (z) direction.
2. The growth takes place in a Newtonian incompressible fluid.
3. The pressure and concentration of the gas inside the bubble equals that at the interface.
4. The liquid is of infinite extent.
5. The gas inside the bubble follows the ideal gas law.
6. Latent heat of vaporization is neglected since it can be assumed that the free gas undergoes a minimal change in temperature upon expansion and the polymer is not considered to be superheated. Thus movement of the gas into the bubble is considered to be completely due to diffusional effects although thermal effects will indirectly affect the growth of the system. An excellent explanation for the validity of this assumption can be found in the work of Arefmanesh et al. [5] which is also supported in other works [96,1].
7. The bubble begins as a nucleus with a spherical shape.

8. Pressure and concentration at the interface are related via Henry's Law:

$$P_g(x,y,t) = K_h C(x,y,t)$$

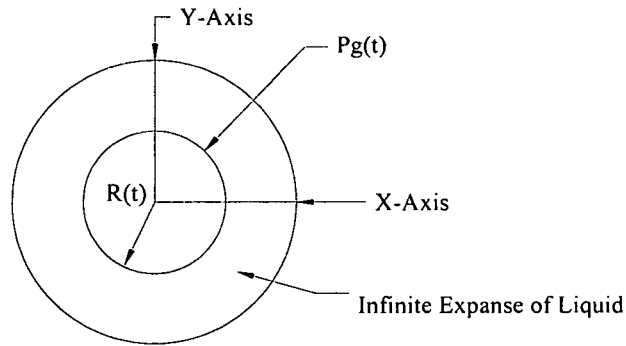


Fig. 3.3 Illustration of the Problem

With these assumptions consider a bubble nucleating and beginning growth at some time $t=0$. According to the assumptions listed above, the equation of continuity with respect to a control surface:

$$\int_{cs} \mathbf{u}_L \cdot \mathbf{n} dS = 0 \quad (1)$$

where \mathbf{n} is the normal vector away from the control surface.

Using the information contained in the equation of continuity, the equation of motion of the liquid melt is written with respect to the control volume as:

$$\frac{\partial}{\partial t} \int_{cb} \mathbf{u}_L dV + \int_{cs} \mathbf{u}_L \cdot (\mathbf{u}_L \cdot \mathbf{n}) dS = - \int_{cs} \mathbf{P} \cdot \mathbf{n} dS + \frac{1}{Re} \int_{cs} \nabla \mathbf{u}_L \cdot \mathbf{n} dS \quad (2)$$

where Re is the Reynolds number.

Using Fick's Law, the equation for diffusion through the melt across the control volume in nondimensional form is:

$$\frac{\partial}{\partial t} \int_{cv} C dV + \int_{cs} \mathbf{C} \cdot \mathbf{u}_L \cdot \mathbf{n} dS = Pe \int_{cs} \nabla C \cdot \mathbf{n} dS \quad (3)$$

where C is the concentration of the gas in the melt and Pe is the Peclet number.

To conclude the mathematical definition of the problem, a momentum balance is taken at the interface. The interfacial momentum balance, also known as the Young-Laplace Equation, relates the pressure difference to the forces acting on the surface of the bubble. In this case, the equation relates the pressure difference across the bubble interface to both the viscous force of the melt and the surface tension of the liquid. This equation takes the form:

$$P_{v,n} - P_{L,n} - \eta \left(\frac{\partial u_L}{\partial \mathbf{n}} \right) = \sigma \left(\frac{1}{R_1} + \frac{1}{R_2} \right) \quad (4)$$

where the pressures are directed normal to interface, R_1 and R_2 are the principal radii of curvature of the bubble, η is the viscosity and σ is surface tension. Simplifying this equation and neglecting the inertial terms leads to [96,119]:

$$P_{v,n} - P_{L,n} + \frac{1}{We} \kappa = \frac{1}{Re} \left(\frac{\partial u_L}{\partial \mathbf{n}} \right) \quad (5)$$

where κ is the curvature of the interface and We is the Weber number.

The initial and boundary conditions applied on these equations are:

$$P_L(x,y,0) = P_a \quad (2a)$$

where P_a is atmospheric pressure

$$P_{Lx}(x_{\max}, y, t) = P_a \quad (2b)$$

$$P_{Ly}(x, y_{\max}, t) = (\alpha * P_a) \quad (2c)$$

where α is a factor greater than unity that drives non-spherical growth by representing the uneven pressure gradient that a bubble is subjected to from different directions along the interface.

$$P_{go}(R_x, R_y, 0) = (\beta \cdot P_a) \quad (2d)$$

where β is a factor defining the initial pressure in the bubble and R_x and R_y are the coordinates of the bubble interface in the x and y directions, respectively

$$V(x, y, 0) = 0 \quad \text{and} \quad U(x, y, 0) = 0 \quad (2e)$$

$$V(x_{\max}, y_{\max}, t) = 0 \quad \text{and} \quad U(x_{\max}, y_{\max}, t) = 0 \quad (2f)$$

$$C(x, y, 0) = C_o \quad (3a)$$

where C_o is the initial concentration of the saturated gas in the melt

$$C(r_x, r_y, 0) = C_i \quad (3b)$$

where C_i is the initial concentration of the bubble interface as related by the pressure via Henry's Law.

$$C(\infty, \infty, t) = C_i \quad (3c)$$

which is a statement that can be made due to the assumption of an infinite expanse of liquid [94]

2.2 Parameters and dimensionless groups

To facilitate the following analysis, the following dimensionless groups are defined.

$$R^* = R/R_c \quad (6a)$$

$$u^* = u/u_c \quad (6b)$$

$$P^* = P/(\rho^* u_c^2) \quad (6c)$$

$$t^* = t/t_c \quad (6d)$$

$$C^* = C/C_i \quad (6e)$$

$$Re = \rho u_c R_c / \eta \quad (6f)$$

$$We = \rho R_c u_c^2 / \sigma \quad (6g)$$

The characteristic radius, R_c , is defined to be the initial radius of the bubble and is assumed to be 1 micron [5]. The characteristic velocity, u_c , accounts for the diffusive nature of the problem and is defined as the ratio of diffusivity to initial radius, D/R_c . The characteristic time, t_c , is also a representation of the diffusive nature of the problem and is defined as R_c/u_c . It should also be noted that employing this scheme results in the Peclet number being 1.

From the list of physical constants listed in table 3.1 of the used material, mesophase pitch, it is seen that the characteristic time for this simulation is 0.001 s. Simulations were run from this point until a maximum of 5 seconds, a point at which it is believed no further growth would occur. Secondly it can be seen that the Reynolds and Weber numbers, even at large bubble sizes, are still less than unity. Consequently, neglect of the inertial terms in equation 5 is valid.

In the work of Hara and Schowalter [36], it was shown that the rheology of the polymer has a distinct effect on the non-spherical nature of the bubble in cavitation phenomenon. During foam processing, a phenomenon different from cavitation, the polymer melt transforms from a viscous liquid to a solid. This transformation, caused by thermodynamic changes in the system,

sustains the polymer in the foam microstructure and like in Hara and Schowalter's [36] work will have a distinct effect on the shape of the bubbles making up the structure. Consequently the changing nature of viscosity during foam processing was incorporated into this simulation by taking the rheological data of Fleurot and Edie [19] and combining it with information acquired using a standard data acquisition system while processing foams using the technique patented by Kearns [42]. This information was combined to obtain a rate of viscosity change with respect to time. The correlation between viscosity and time was determined to be:

$$\eta = \eta_i + 15.6t \quad (7)$$

where t is the time in seconds and η_i is the initial viscosity.

Table 3.1 Physical constants of mesophase pitch used in simulation

Parameter	Value
D	$1 \times 10^{-9} \text{ (m}^2/\text{s) [96]}$
K_h	$4.73 \times 10^{-5} \text{ (mol/N m) [96]}$
C_i	$478 \text{ (mol/m}^3 \text{) [96]}$
η_i	46 (Pa s) [19]
σ	0.035 (N/m) [3]
ρ	$1260 \text{ (kg/m}^3 \text{) [118]}$
R_c	$1 \times 10^{-6} \text{ (m) [5]}$
u_c	0.001 (m/s)
t_c	0.001 (s)

2.3 Numerical solution of the governing equations

Based largely on the work of Ye et al. [119] and Ye et al. [118], the numerical solution used in this study is founded in an interface marker methodology working in conjunction with a grid reshaping procedure. The method is chosen due to its ability to handle any degree of complexity in the shapes of the interface along with its second order accurate solutions to the governing equations. Details of its implementation are given below.

2.4 Interface and grid reshaping to solve governing equations

At the onset of the solution, the initially spherical bubble is placed on top of the standard Cartesian grid. This interface, while not extremely complex, provides problems in the solution of each of the governing equations. The difficulties arise due to the fact that basic linear interpolation of the gradients and fluxes in cells that are adjacent to the interface, regions of the utmost importance in the model, are not of second order accuracy if a linear interpolation scheme is employed. In fact in many cases points adjacent to these special cells do not even lie on the same side of the interface as shown in figure 3.4.

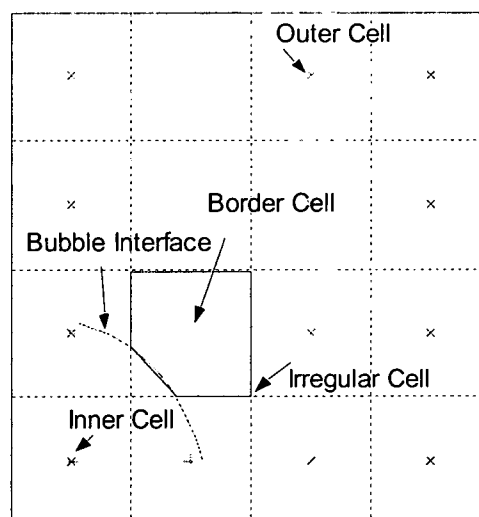


Fig. 3.4 Sample Grid

In order to solve these difficulties, the grid is reshaped to account for the shape of the interface. The reshaping takes place by first identifying on which side of the interface each cell center point lies. Knowing which side of the interface the point resides, the point is then further categorized in one of three ways: a point inside the bubble, a point in the liquid melt adjacent to the bubble interface, and finally a standard point outside the bubble. Obtaining information concerning placement of the cell centers is developed using the work of Udaykumar et al. [106].

Knowing the shape of the interface, obtained through interpolation functions drawn through the marker points, a process that will be described in detail in the coming section, the grid is now ready to be reshaped. The grid is only reshaped in the immediate vicinity of the bubble where the cell centers have been labeled as border points. On these border points the intersection of the interface and the cell is calculated. The shape of the cell is then

modified into a trapezoid to account for these intersections. Limits on this reshaping procedure allow cells to only become 0.5 to 1.5 times the size of a standard cell. The result of this reshaping procedure leaves a grid that is composed of almost completely squares and trapezoids although triangular cells are possible.

In regions where the interface does not affect the shape of the cell, fluxes and gradients can be solved using basic linear interpolation. However as stated earlier, this linear interpolation cannot be used in the irregular cells. Instead a second-degree polynomial method that interpolates the flux through an irregular cell is adopted. This method uses an interpolating function in conjunction with a six-point stencil to obtain fluxes to second order accuracy [118]. It should be noted that although in this study only one bubble interface is accounted for, the method employed capable of handling multiple interfaces and can even be used in three dimensions.

With the grid reshaped, the numerical solution begins by solving the momentum equation in a fractional step manner. Using this method the advection diffusion portion of the momentum equation is calculated first insuring momentum conservation in each cell. Then the pressure-poisson portion of the equation is solved assuring mass balance and after only a few iterations the flow field is sufficiently calculated. In solving of the system, a variety of different solution procedures were attempted ranging from a successive over-relaxation method to a Bi-Conjugate Gradients Squared method. It is found, however, that in order to minimize computer time, as well

as maximizing accuracy, a subroutine for solving matrices included in Matlab, the language used in this program, is working optimally.

With the flow field now solved, both the mass diffusion of the gas through the melt and the Young-Laplace equation (stress balance equation) are solved. The solutions of these equations then give a sufficient amount of information to update the boundary and begin the next iteration of the process.

2.5 Reshaping of the boundary

Drawing an interpolating curve through marker points that are spaced at a prescribed distance over the interface shapes the boundary. In this instance, a second-degree spline curve is employed to draw the interface of the bubble between the marker points. A second-degree polynomial is utilized, as there is no inherent advantage in the computation of the solution in using a third degree curve [105].

The movement of the marker points tracks the changing position of the interface and is computed through use of the Young-Laplace equation. The values at the marker points, known through the prescribed Dirichlet boundary conditions, are used in conjunction with those values computed for the border cells closest to the marker point being considered. The marker point is then moved to insure mechanical equilibrium in the system and then after each marker point has been updated accordingly the interface itself is redrawn. Due to this expansion of the bubble's size, the pressure inside the bubble must decrease as well. Consequently, the pressure inside the bubble is

updated to be in equilibrium with the melt at the new location of the interface. This process is repeated throughout the entirety of the solution.

Due to the assumption of an infinite extent of liquid melt, the concentration gradient only serves to show where the blowing agent is incorporated into the melt most quickly. Since there is an infinite amount of gas this equation is not needed to constrain the growth to account for decreases in the amount of vapor available for the bubble to absorb. Therefore in this model, its main purpose is to illustrate where in fact the most absorption takes place.

3.0 Results

Employing a 100X100 grid, where each cell side is of equal length to that of the critical bubble radius, bubble growth is solved using the technique described in the previous section. Time scales on the order of 10^{-3} to 5 seconds are examined. All simulations were performed for a sufficient amount of time such that one of two limiting cases occurred. First, growth was allowed to occur until the bubble's largest radius (R_x) reached 100 microns, a size which few bubbles in actual foams grow larger than. Secondly, growth was allowed to occur until the viscosity reached such a value that growth no longer occurred at appreciable levels.

Using an initial pressure inside the bubble higher than that of the surroundings, growth is simulated and the degree of non-spherical behavior is investigated along with flow around the bubble interface and diffusion of the saturated gas through the melt. Employing differing boundary conditions for pressure at the top and side of the grid, P_{bndy} and P_{bndx} , respectively, drive

non-spherical growth. In the employed model, P_{bndy} is set five times that of atmospheric pressure while P_{bndx} remains at atmospheric pressure. With this pressure imbalance at the boundaries, growth occurs at a more rapid rate along one axis and leads to bubble growth which is almost elliptical in shape. Figure 3.5 shows the growth rates of the bubble in the x and y directions. It should be noted how similar growth mirrors that of the standard $t^{1/2}$ trend [5,107]. This comparison displays the accuracy of the present model and its results. With a change in boundary conditions for P_{bndx} and P_{bndy} to equal values, spherical growth ($R_x=R_y$) is simulated and again grows to the established $t^{1/2}$ rate as well.

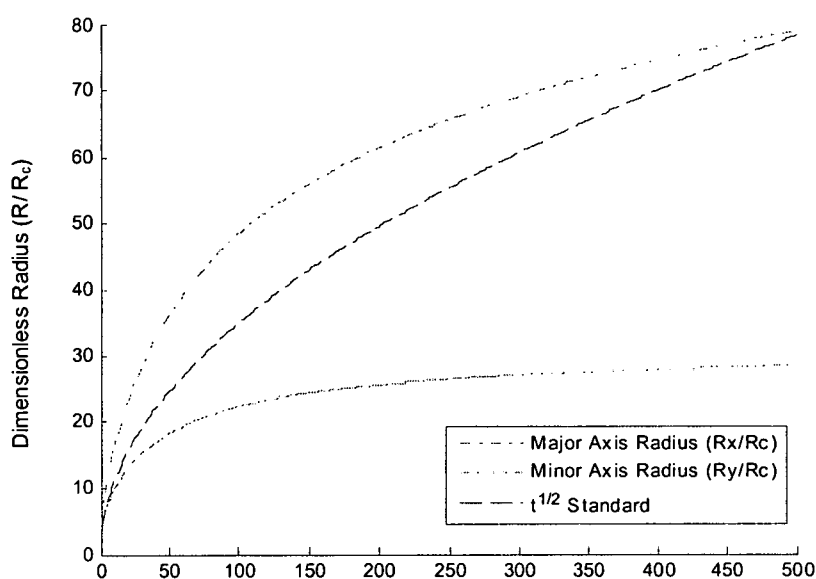


Fig. 3.5 Bubble growth vs. time

It should be noted the more rapid growth along the major axis of the bubble. This is due first to the larger pressure gradients that are present along the interface of the bubble and the boundary in this direction.

Secondly, it is also a consequence of assuming an infinite pool of saturated gas for the bubble to absorb. With this infinite amount of absorbing species present, there is nothing of equivalent magnitude to retard the growth driven by the large pressure gradients. Contrarily, along the minor axis of the bubble, pressure gradients are smaller originally and reduce at a quicker rate than on the major axis resulting in less rapid growth. These two different pressure gradients lead to a bubble that is non-spherical. This non-spherical behavior as a function of time is displayed in figure 3.6.

The non-spherical growth characteristics of the bubble are at the center of interest in this study for with an understanding of controlled non-spherical growth is the opportunity to make tailorable foam. To examine this type of growth further, simulations are performed with variations of the initial bubble pressures (P_{g0}). As expected, growth rates as well as final sizes of the bubble increase as a result of the higher initial pressure, a fact that can be seen in figure 3.7. Interestingly, the non-spherical shape is more eccentric as the initial bubble pressure is lowered. These results can be seen in figures 3.8 and 3.9.

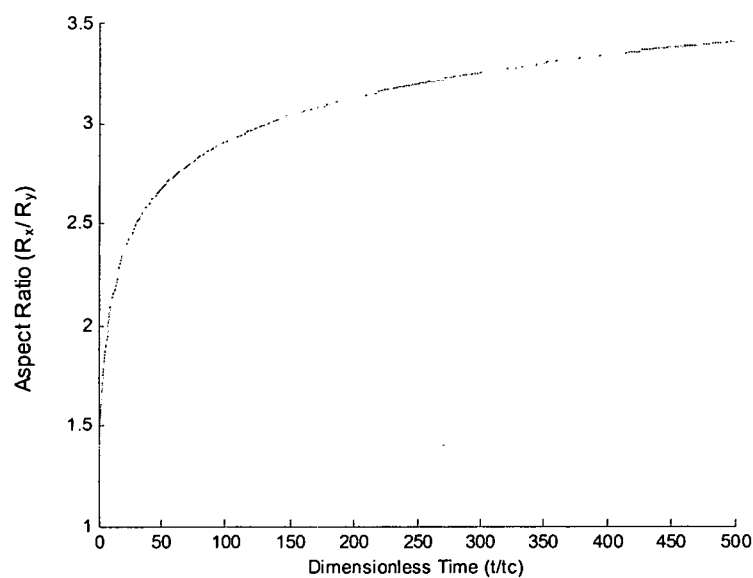


Fig. 3.6 Non-spherical growth vs. time

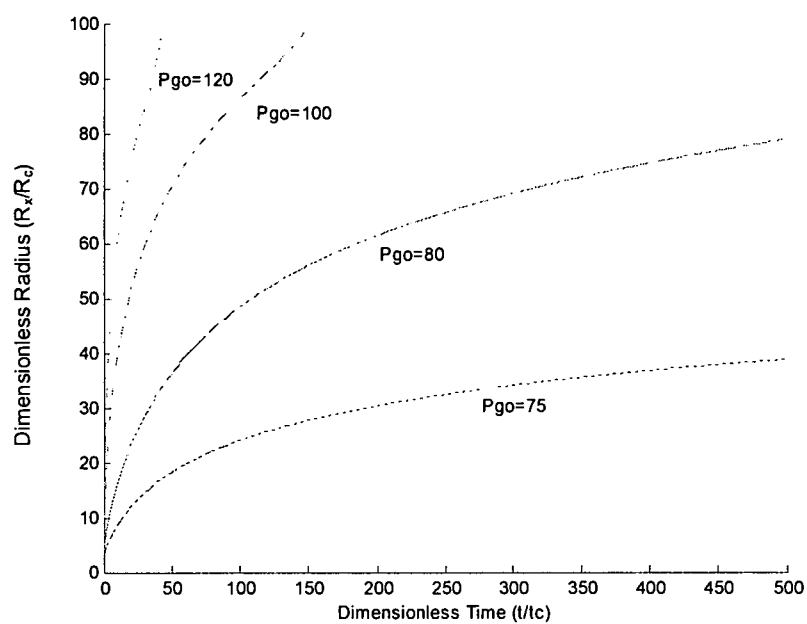


Fig. 3.7 Effect of initial pressure on growth

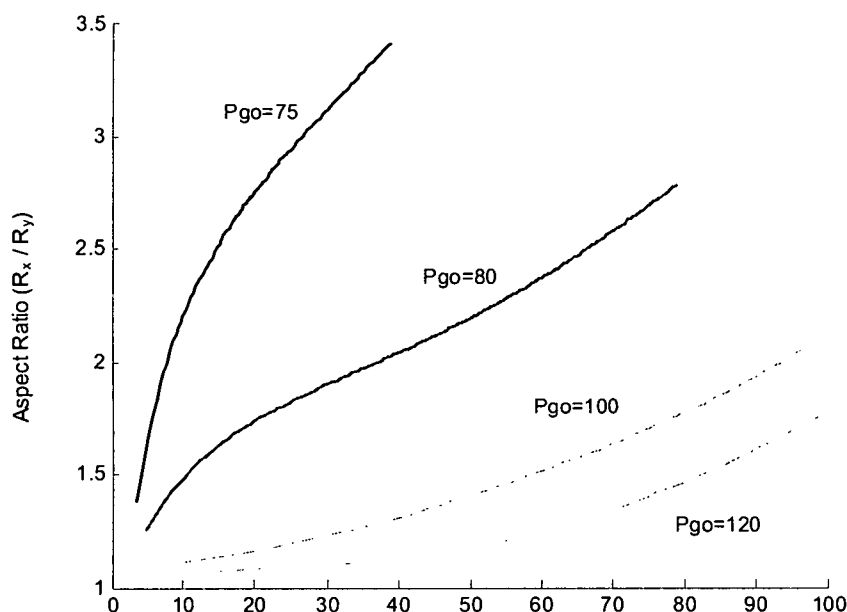


Fig. 3.8 Effect of initial bubble pressure on non-spherical behavior of bubble

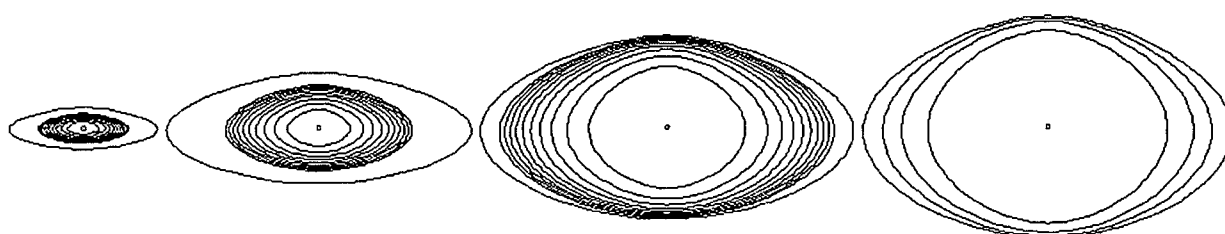


Fig. 3.9 Effect of P_{go} on final bubble size and shape (note: Increasing P_{go} follows a left to right trend. Lines were drawn at each 0.01 s of growth until 0.1 s. The final line represents the bubble at end of growth period)

It is interesting to examine why in fact non-spherical growth is more pronounced when a lower initial bubble pressure is used as an initial condition. As stated previously, growth occurs as a result of a pressure imbalance between the liquid and vapor interface. This pressure imbalance is dependent upon the pressure of the liquid melt at the extremes of the grid as

well as the initial bubble pressure. Non-spherical growth occurs as a result of the pressure gradient between the liquid and the vapor being unequal at differing places along the surface of the bubble. Even though these unequal pressure gradients are present at all initial bubble pressures, non-spherical growth is mitigated as $P_{go} \gg P_{bnd}$ even though P_{bndy} is five times greater than P_{bndx} . Consequently, it can be concluded that more eccentricity in the shape of the bubble is attained as the initial bubble pressure is lowered and the initial pressure imbalance at the interface is increased. The pressure difference is greatest at the earliest times of growth, when viscous forces are at their smallest and thus Reynolds and Weber numbers can be assumed to be at their largest magnitudes, and thus the non-spherical behavior is most affected at these earliest times as can be seen in figure 3.8.

Additionally the effect of viscosity is examined in the system. In the past examinations of foaming phenomenon the parameter has largely been ignored, yet in the work of Hara and Schowalter [36] viscosity was shown to have a distinct effect on the non-spherical behavior of bubbles in cavitation phenomenon. Consequently, simulations are performed in this study that examine the effect of rate of viscosity change on the non-spherical behavior of the bubble. This rate of viscosity change is temperature dependent and therefore it is logical to believe that assumption 6 will lead to erroneous data in this instance. Arefmanesh et al. [5] asserted that these assumptions only lead to quantitative errors while the qualitative aspect of the analysis remains accurate and thus information in this simulation can be gathered in its present

form. With this in mind, the rate of viscosity change was examined by doubling and halving the derivative with respect to time of equation 7.

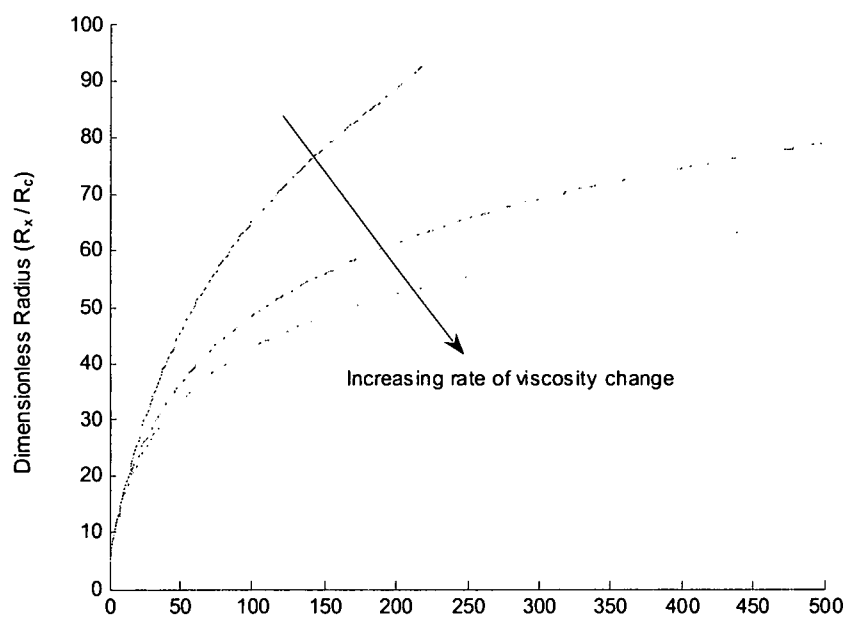


Fig. 3.10 Effect of $d\eta/dt$ on final bubble size

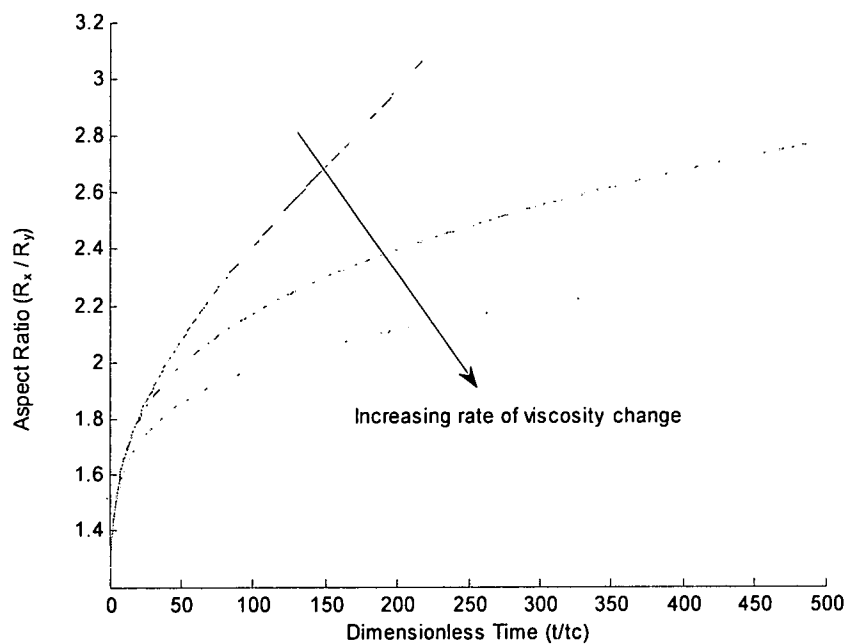


Fig. 3.11 Effect of $d\eta/dt$ on final bubble shape

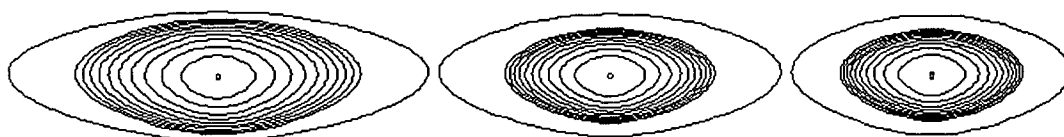


Fig. 3.12 Effect of $d\eta/dt$ on final bubble size and shape (note: Increasing rates of viscosity change follow a left to right trend. Lines were drawn at each 0.01 s of growth until 0.1 s. The final line represents the bubble at end of growth period)

From figures 3.10, 3.11, and 3.12, the distinct effect of viscosity can be seen on the system. As viscosity increases, growth is reduced substantially. The viscous forces dampen growth by severely mitigating the pressure difference between the bubble and liquid melt and eventually terminating growth and freezing the bubbles in a certain arrangement. Therefore it is of no surprise that this effect is exaggerated as its rate of increase is heightened. More importantly the shape of the bubble is highly dependent upon the viscosity as well as can be seen in figures 3.11 and 3.12. With increased viscosity, non-spherical behavior is damped due to the fact that the large viscous forces diminish the effect of pressure imbalances along the interface leading to minimal growth on either axis. In fact, it was found that until the major radius (R_x) reached a size of $65 \cdot R_c$, each of the bubbles had approximately the same non-spherical behavior. It was only after this point that a major difference in non-spherical behavior occurred due to growth on either axis being practically terminated at higher viscosity rates of change. Consequently, there is a critical region where viscous forces dominate the system to such an extent that pressure differences along the interface, and thus non-spherical growth, are minimized to a point where the extremely minimal amount of growth still occurring can be considered almost spherical.

Finally the effect of initial bubble radius on both growth and non-spherical behavior of the bubble is displayed in figures 3.13-15. Shafi and Flumerfelt [96] asserted that growth is dependent upon the initial bubble radius due to the perturbation that this initial size places in the thermodynamic balance of

the system. In this simulation, where critical radii (R_c) were set from 1 to 2 microns, the distinct effect of initial radius can be seen. As seen in figure 3.13, growth rates as well as final sizes of the bubbles increase with an increase in the initial radius, a trend that is supported in the work of Shafi and Flumerfelt [96]. This trend occurs as a result of the extra energy the system initially encompasses with larger initial bubble sizes.

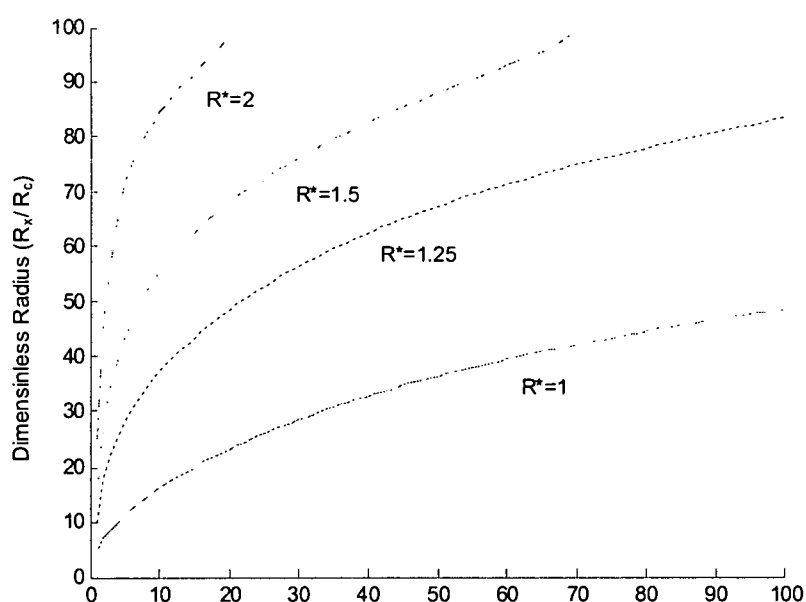


Fig. 3.13 Effect of initial radius on bubble growth

From figures 3.14 and 3.15 the effect of the initial radius on non-spherical behavior are seen. The amount of non-spherical behavior seems to be directly related to the size of the initial radius as larger initial radii develop more spherical bubbles. This trend is a result of the pressure gradient imbalances along the surface being mitigated at the earliest times of growth when the Reynolds and Weber numbers can be assumed to be at their highest values. After this initial stage of growth, the time when the effects of

viscous forces are at their smallest and growth rates conversely at their highest, non-spherical behavior for all radii then proceed at approximately the same rate as viscous forces begin to dominate the system and the pressure imbalance across the surface of the bubble is most acutely seen. This effect is seen in figure 3.14 which illustrates the latter stages of growth where the change in shape with respect to major radius is approximately equal for all radii considered.

From the investigation of initial radius and bubble pressure, growth is seen to be most non-spherical when viscous and surface tension forces dominate growth. Conversely this was not the case in the examination of rate of viscosity change as high rates of viscosity change minimized growth on either axis of the bubble thus limiting its non-spherical nature. Therefore, this study contends that the most non-spherical of bubbles will occur when parameters encompassing both Reynolds and Weber numbers are chosen as to minimize these dimensionless groups while remaining below a critical region above which growth does not occur appreciably in any direction.

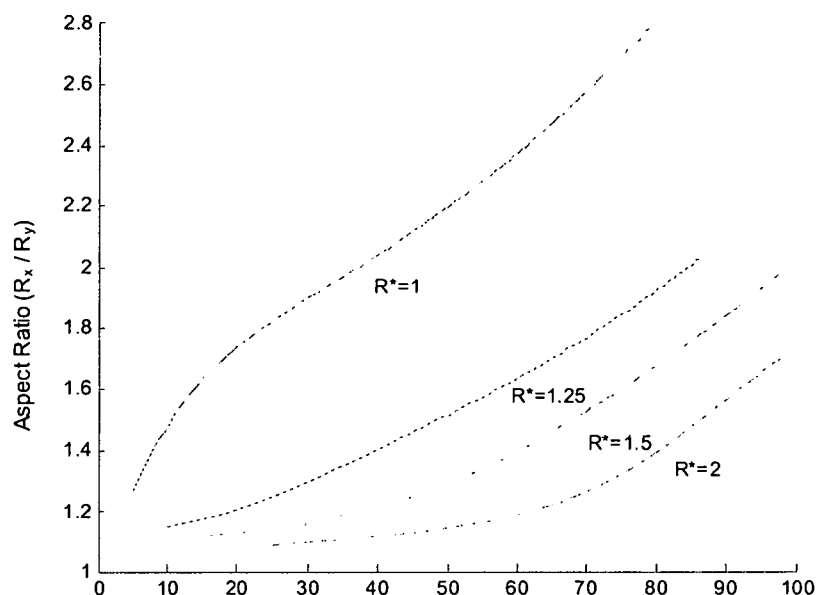


Fig. 3.14 Effect of R_0 on final bubble shape

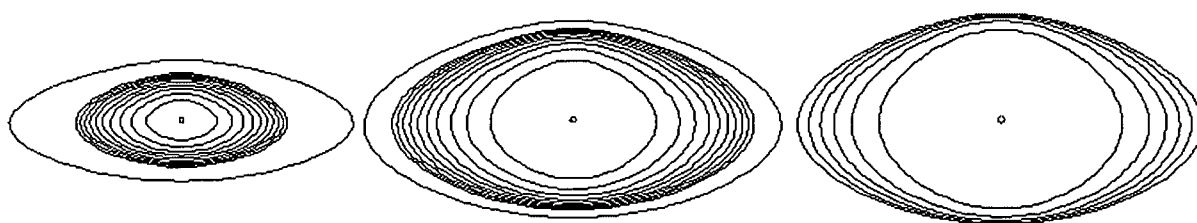


Fig. 3.15 Effect of R_c on final bubble size and shape (note: *increasing initial radius follows a left to right trend. Lines were drawn for each 0.01 s of growth until 0.1 s. Final line represents the bubble at end of growth period*)

4.0 Conclusions

A numerical procedure for the prediction of non-spherical bubble growth assisted for carbon foam fabrication is presented. The procedure uses a transforming Cartesian grid method with marker points to balance mechanical forces and track bubble growth. The model's accuracy is illustrated through its conformation to the $t^{1/2}$ standard. Parametric changes not only affect growth as previously reported but also have significant effects on the final

shape of the bubble. Increasing initial pressure and radius in the bubble lead to a reduction in the non-spherical behavior of growth. Finally in this work, rates of change in viscosity were accounted for and found to have a substantial damping effect on both the growth and non-spherical behavior of the bubble.

From knowledge obtained in this study a greater qualitative understanding of bubble shape during growth is obtained. This understanding will lead to foams that are tailorable to specific applications thus maximizing the potential of carbon foams. With the knowledge obtained in this study, future work can now be initiated on a similar numerical model concerning the influence of additional bubbles on non-spherical growth in order to further deepen the knowledge concerning the topic of controlled bubble growth.

Chapter 4

Carbon Foam Mechanics: Examining the effect of nanofibers on localized and bulk properties

1.0 Introduction

A cellular material made from a pitch based precursor, carbon foam has emerged as a material of great promise due to its extremely high specific properties. With a specific thermal conductivity over 4 times that of copper and a specific modulus rivaling that of a Kevlar honeycomb, carbon foam has been suggested for a myriad of applications spanning a wide spectrum from the leading edges of high performance aircraft to a material for use in internal prostheses [87,105]. The foam's unique and wide-ranging properties arise as a result of an interconnected three-dimensional graphitic-like microstructure arranged in a cellular fashion [2,29,30,31]. This microstructure results in performance that deftly incorporates the advantages inherent in both cellular and carbonaceous materials.

Carbon foam is acquired through careful control of thermodynamic fluctuations when a pitch-based material is heated above its melting temperature. In one form of processing, this occurs through a sudden release of pressure in a supersaturated solution of gas in a molten precursor [41,42].

As a result of the thermodynamic perturbation of the pressure release, bubbles form and expand in the molten precursor forming the cellular nature of the subsequent foam. The manner and extent to which these bubbles grow determine the foam's microstructure and hence the thermal, electrical, and mechanical properties of the final material.

The mechanical properties of cellular materials are complex, dependent upon both the material itself as well as its microstructural arrangement. Consequently, a dearth of work has been dedicated to examining the microstructure of cellular materials in order that properties might be correlated to the bulk material itself. First among these studies was the work of Lo in the early 1960's who related the idealized cellular microstructure to the packing of spheres to define the unit cell [72]. In this arrangement, the deformation of the ligaments, defined as the intersections of the spheres, was solved using beam theory. The alignment in the unit cell of these ligaments determined whether the cell fractured due to a bending or stretching mechanism. Using this method, Lo asserted that equivalent modulus and Poisson ratio of the foam could be related to the bulk material properties in an inverse linear relationship to the porosity [72]. Christensen later supported this relationship by deriving a similar expression when ligaments are randomly dispersed and deformation assumed to occur only in an axial fashion [9].

Gibson and Ashby, in the keystone argument in the subject, then revised this relationship by assuming that deformation would be much more likely to occur in bending due to shear. Using a trigonal arrangement of ligaments to

model the unit cell, it was found that the equivalent modulus of the foam with respect to the bulk material's properties was proportional to the porosity squared [25].

In carbon foams, however, it has been shown that the ligaments form a tetrahedral unit cell rather than the trigonal arrangement assumed by Gibson and Ashby [2,29]. This difference in truss structure was shown to be of diminutive importance as Warren and Kraynik proposed a very similar relationship to that of Gibson and Ashby of effective modulus and Poisson ratio using a tetrahedral unit structure under realistic assumptions of imperfect unit cell arrangement [111,112]. Working from these two studies, then allowed Hall and Hager to assert that the bulk modulus of carbon foam is insensitive to local cell geometry but instead chiefly dependent upon the porosity of the foam, a conclusion very similar to that relationship which was originally proposed by Gibson and Asby [34].

It should be noted, however, that prediction of the overall bulk foam properties in this study and the host of subsequent predictions was based on uniform ligament properties equivalent to P-100 carbon fibers [34, 94]. This assumption of uniform carbon fiber like ligament properties has long served as the foundation in arguments for carbon foam viability yet to the present its validity has hardly been examined.

Under polarized light microscopy, however, it is obvious that this assumption is not valid as ligaments of pitch derived carbon foams show variances across the ligament. Sihn and Roy tackled a portion of this problem

in a study performed in 2004 [94]. Using a tetrahedral unit cell similar to the one developed by Hagar in 1992, Sihn and Roy varied the properties across the ligament and modeled deformation using finite element analysis. Through this study, it was reported again that bending dominates as the deformation mechanism and furthermore that effective modulus is most dependent upon the transverse properties of the ligaments. Consequently, processing schemes improving this property would most effectively improve carbon foam performance. Yet even with the enhanced analysis of Sihn and Roy, ligament properties were still assumed to be similar to that of carbon fiber, an assumption that will be shown to be tenuous in the following section.

1.1 Microstructure of Graphitic Foams (Orientation and Disclinations)

Due to the fact that graphitic foam is solely made of carbon atoms, it has been thoroughly propounded that interconnected ligament networks of these aligned graphitic sheets may achieve properties equal to that of high performance graphite fibers [2,73,115,121,122]. Consequently, under conditions of precursor uniformity, graphitic foams' performance, like their fiber brethren, is directly related to the basic cell structure of the carbon molecules. More simply, it is the molecular orientation and crystallinity of the foam's ligaments and nodes that governs the mechanical and thermal capability of the material. Therefore, it is this orientation and crystallinity that determines if a foam will have capability equal to that of carbon fiber.

To examine orientation, a series of carbon foams were produced using the U.S. Air Force blowing process [42,43]. The foams were made from 100%

mesophase synthetic pitch (Mitsubishi ARA 24 resin) using a nitrogen blowing gas to a bulk density of $\sim 0.3 \text{ g/cm}^3$. The foams were then stabilized in an air oven at 170°C until a 6% weight gain was accrued at which point the foams were heat-treated to a temperature above 2500°C insuring graphitization. After each heat treatment, the samples were characterized using microscopy techniques.

The changes in the molecular structure of any graphitizable carbon due to heat treatment are well understood [13,115]. As the heat treatment progresses, the carbon skeletons become very straight and stiff reaching the minimum interlayer spacing of the graphitic structure, a process which is seen in Figure 4.1. These changes in molecular structure cause predictable changes in the crystallinity of the carbon artifacts.

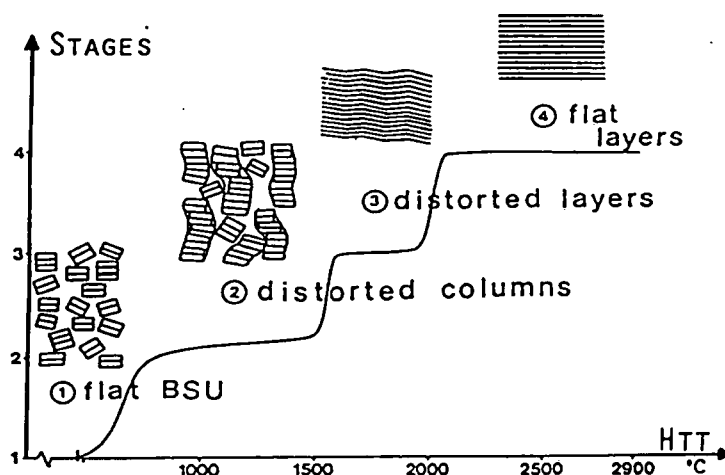


Fig. 4.1 Structural changes as function of heat-treatment temperature [115].

Disclinations are abundant features which affect the performance of any carbon microstructure. They are produced during the formation and

subsequent deformation of Brook and Taylor mesophase spheres (discotic nematic liquid crystal). Typical disclinations, i.e. wedge or twist as shown in figure 4.2, have various strengths and are retained as polymerization continues as the carbonaceous mesophase hardens as coke. With further heat treatment, ordering of the layers to obtain the graphitic atomic structure occurs whereupon the disclinations formed remain, unable to annealed out, in the heat-treated solid matrix. These disclinations serve as an important parameter in the performance of carbonaceous materials as the studies of White and Zimmer display [115,121,122].

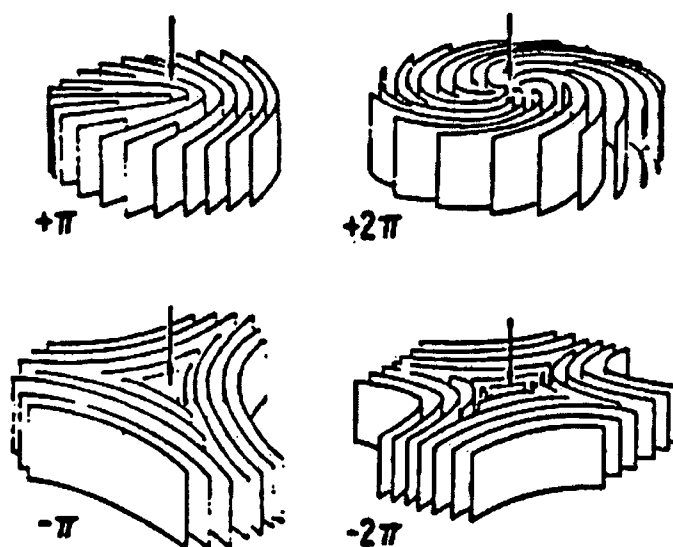


Fig. 4. 2 Disclinations in carbonaceous mesophase. In this figure, the layers represent the general preferred orientation of the platelike molecules of the discotic nematic liquid crystal.

Figure 4.3 shows a general view of as processed carbon foam. A wide range of bubble sizes as well as thicknesses and elongation of both the nodes and ligaments are observed to vary from one location to another as is seen in figures 4.3a and 4.3b. In general, the ligaments are homogeneous with a preferential orientation containing some disclinations more or less

oriented as seen in figure 4.4a. However, the ligaments seem to be free of disclinations when they are extremely thin (Figure 4.4b). Nodes, on the other hand, regardless of size, exhibit a much higher occurrence of disclinations as shown in figures 4.5a and 4.5b.



Fig. 4.3 (a) Low magnification optical micrograph of carbon foam (b) Optical micrograph showing both ligament and node



Fig. 4.4 (a) Ligaments with disclination (b) Ligaments with disclination



Fig 4.5 (a & b) Nodes with disclination

After carbonization and graphitization heat treatments, two types of ligaments are clearly distinguishable: one that is homogenous, thin, free of disclinations and highly oriented while the second type of ligament includes some disclinations and cracks. The nodes, on the other hand, are on average full of disclinations with a large random orientation of the graphene layers. Figure 4.6 shows a graphitized foam where both types of ligaments are present, delineated by single arrows, as well as nodes distinguished using double arrows. A single ligament relatively free of disclinations, circled in figure 4.6, was then chosen for high magnification analysis as almost all nodes and ligaments are thin enough for TEM examination.



Fig 4.6 Bright field image of graphitized foam. TEM sample preparation was performed using an atomic milling technique.

Figure 4.7a shows the 002 dark field where the stacks seen edge-on are imaged as bright domains as they better fulfill the Bragg condition. Furthermore, the edges continue to be bright even when departing from the Bragg condition as is seen in figure 4.7b due to increasing tolerance. Consequently in studying these bright regions, it is readily apparent that a parallel situation as seen in carbon fibers is occurring where there is true alignment of the graphene layers along the ligament axis as denoted by the arrows. The extension and the perfection of these graphene layers vary from the interface node-ligament area to center of the ligament indicating once

again the variance in expected properties across the ligament. Figure 4.7c then gives confirmation of the lack of disclinations as all 001 reflections from 002 to 0014 are seen spread into arcs.

In figure 4.8, another type of ligament is shown in which the concentration of wedge and twist disclinations is considerable. In these types of ligaments there remains a high degree of graphene sheets parallel to the ligament axis, but this preferred orientation is continually interrupted by various disclination defects as displayed in figure 4.8. In this case a $-\pi$ disclination is observed although within a given grain, the alignment of the graphene layer remains perfect as shown by the single arrow in the figure. These disclinations are not of the high strength variety as this research group has never observed one of strength greater than 1, a consequence of their proclivity to disassociate to a lower energy as the square of strength is proportional to energy.



Fig 4.7 (a) and (b) 002 dark field and bright field images of ligament relatively free of disclinations (c) selected area diffraction of centered area of ligament free.



Fig. 4.8 High resolution image of areas on the ligament showing preferential orientation and $-\pi$ wedge disclination

From this analysis, it can be stated that disclinations, just as in all graphitic materials, play a prominent role in foam performance. The type and distribution of these disclinations could determine the foam's physical performance in such manners as fracture toughness and thermal conductivity. In this analysis, examples of low- and high-resolution electron microscope lattice images of a variety of ligaments and nodes have been shown in which two differing types of ligaments have been identified. One type of ligament is free of disclination defects with an excellent orientation of graphene layers parallel to the ligament axis. Conversely, the second type of ligaments is full of disclinations of differing types and cracks although the graphene layers continue to, on average, be aligned with the ligament axis. The concentration of these disclinations and their orientation is dependent on material precursors and foaming conditions but is not further examined in this work.

These disclinations and high regions of graphitic order lead to foams which have lower bulk mechanical performance than that predicted by researchers who assumed foams to be composed of carbon fiber like ligaments. Consequently, to enhance foam mechanical properties similar thoughts and processes used to improve carbon fiber performance should be utilized.

Most carbon fibers exhibit a Young's modulus ranging between 500-900 GPa and tensile strength of 5 GPa [115]. The high value of the fiber's modulus is related to its graphitizability while the strength is due to folding and zigzag structure which is shown in figure 4.9a and 4.9b. This zigzag texture

plays a key role in preventing glide of the 001 plane in graphitic materials and enhances the tensile strength properties of carbons through an interlocking mechanism of the graphene layers. The same mechanism explains the mechanical properties of carbon whiskers and high-modulus carbon fibers. Consequently, to obtain the types of strengths predicted and hoped for in foams, this type of zigzag structure must be present in the ligaments. This work adds nanofibers to the pitch matrix in order to achieve foam ligaments with this carbon fiber like morphology.

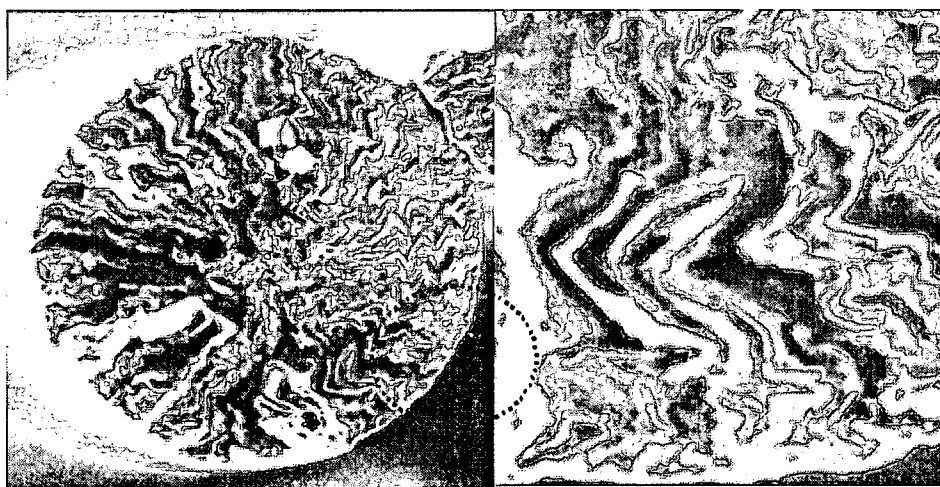


Fig 4.9 (a) Cross section of pitch based carbon fibers. (b) High resolution imaging of areas of folding and ziga-zag textures (circled area in Fig. 10a).

Consequently in our analysis carbon nanofiber is incorporated into the pitch-based precursor prior to the foaming operation in order to produce a cellular carbon-carbon nanocomposite [48]. Carbon nanofiber's attractiveness lies both in its high strength, reported to be over an order of magnitude higher than steel, as well as its tailorable electrical properties, opening the possibility for multifunctional foams [77]. The nanofibers,

composed of rolled up graphite layers, if integrated successfully, have been predicted to increase the strength and modulus of many types of composites including foams [77,97,104].

Inclusion of the nanoconstituent into the composite is not trivial, however, as several issues have been reported to have a deleterious effect on nanocomposite performance. Uniform dispersion of the nanoconstituent into the composite has been shown to be problematic, as several studies have reported degradations in strength of the composite with nonuniform incorporation [97,104,83,26]. Without uniform dispersion, the nanofibers agglomerate into bundles, bundles which offer very little strength as the individual tubes do not bond together but instead slip past one another [104, 97]. In addition, as is the case in any composite, interfacial issues are integral to success as well [97, 104, 83]. This problem is believed to be of smaller consequence in this instance due to the matching composition of both matrix and fiber [26].

In response to these issues, this paper attempts to qualitatively examine these challenges with respect to cellular materials, a class of materials yet to be characterized as part of a nanocomposite. This characterization was carried out by preparing a series of foams doped with carbon nanofibers of both various types and weight percentages. These foams were then mechanically tested to examine the effect of both weight percentage and structure of the nanodopant on the strength of the carbon foam.

Two types of tests were performed to assess this effect. First a standard bulk compression test was performed in order to examine how the cellular material reacted under load. Furthermore, this is the benchmark test for cellular material and thus serves as a manner to compare the present foams to that of its predecessors.

Secondly, a series of tensile tests were performed on individual foam ligaments. These single ligament tests were considered as most models have assumed ligament strength on an equal level to high performance graphitic fibers rather than using an experimentally obtained measure [94,95]. In addition, in utilizing only an individual ligament the loading conditions will be simplified thus giving insight yet to be proffered on carbon foam fracture mechanics.

In utilizing these two different tests, information will be obtained regarding both failure mechanism of this unique cellular material, carbon foam. In addition, for the first time the mechanical behavior of a cellular carbon carbon nanocomposite will be examined. In this examination, the effects of nanofiber structure, dispersion, interfacial bonding, and alignment will be attained with respect to a cellular material in nanocomposite form. Through this information processing of the nanocomposite foams can be optimized to increase mechanical performance of this next generation cellular material.

2.0 Experimental

2.1 Acquisition of Testing Samples

A synthetic mesophase pitch precursor was jet-milled to the prescribed size of 5 μm according to the methods described by Kearns' patent [42]. Meanwhile, in a separate procedure, the carbon nanofibers were shear mixed for 30 minutes at 1800 rpm under an acetone bath to diminish clumping. Once mixed the acetone was allowed to naturally evaporate with the now dispersed nanofibers ready for combination with the pitch precursor.

Nanofibers of type PR-19-PS, PR-19-LHT, and PR-19-HHT, were then combined with the pitch precursor at percentages of 0.5-5% by weight [85]. The powdered combination of pitch and nanofiber was then thoroughly blended under agitation by a high rpm electric mixer for over three minutes with manual mixing interspersed at 30 second intervals to prevent clumping of the powders, insuring as great a uniform dispersion as possible. The mixture is then pressed into a solid perform under 24,000 psi using a standard hydraulic press whereupon the form is ready for the foaming process.

The foaming process takes place in a small Paar pressure reactor, 75 in³, fastened to a standard data acquisition system connected to a PC. The mixed preform is placed 1 in. below the reactor's thermocouple whereupon the reactor is sealed and purged of all atmospheric air using a nitrogen blanket for 30 minutes. After purging, the system is then pressurized at which point the system is subjected to heating at a rate of 4°C/min until the foaming conditions of 275°C and 1000 psi are attained. These foaming conditions

were chosen after preliminary studies indicated that the most uniform of foams using the precursor were obtained at these conditions. A study of this uniformity is given in chapter 5. With the foaming conditions now met, temperature and pressure are held for 20 minutes to assure steady state conditions at which point the pressure is rapidly released to induce foaming.

After foaming, stabilization was accomplished using a procedure identical to the one outlined in chapter 1, section 2.3.1. The foams were then carbonized using a heating rate of $4^{\circ}\text{C}/\text{min}$ to a temperature of 1000°C where they were held for one hour and the temperature was then allowed to decrease at a rate equal to the original heating.

After carbonization, the foam samples were then machined into 0.5 in^3 blocks as specified by the testing standard for bulk compression. Single ligaments were obtained mechanically as well through manual extraction using a razor blade. Only ligaments having a weight percentage of 5% nanofiber were examined in order to maximize the probability of nanofiber effects due to the samples extremely small size.

2.2 Test Method: Bulk Compression

Using ASTM-C1424-99, each of the carbonized foams were compression tested. A 6000 lb load cell was used to measure the deformation of a 0.5 in^3 cube of carbon foam under a crosshead speed of $1\text{ mm}/\text{min}$. Measurements were taken until the foam densified according to the definition of Gibson and Ashby [25].

2.3 Test Method: Ligament Tensile Test

The single ligament tensile stage, shown in figures 4.10 and 11, designed and fabricated by our research team, consists of a 50-gram load cell connected to a stationary sample plate. The stationary sample plate stands directly opposite another sample plate which provides the linear motion imperative for the testing to occur. Motion takes place through the use of a stepper motor connected to a loading arm through the utilization of a microfabricated-threaded shaft.

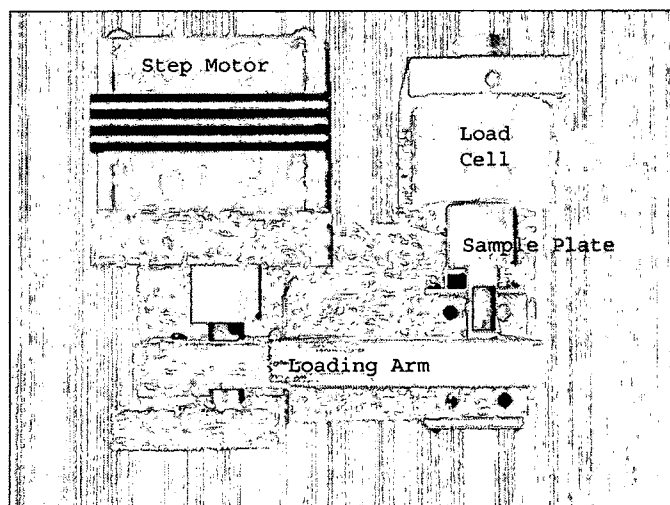


Fig. 4.10 Top view of ligament loading stage

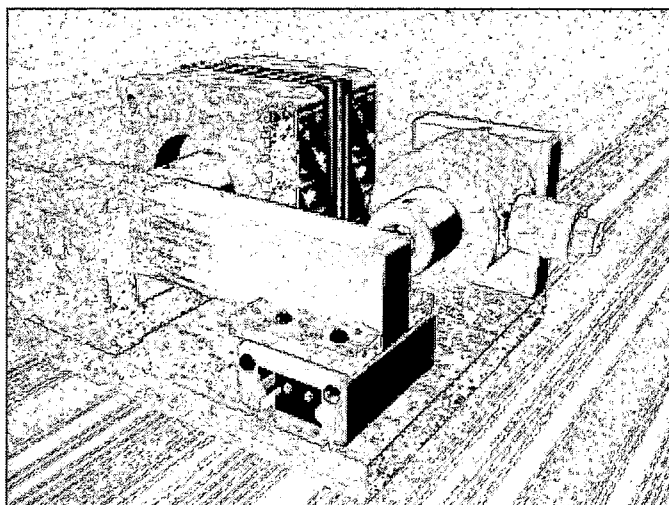


Fig. 4.11 Ligament tensile stage

Made from a ThorLabs fine adjust screw, the shaft is connected through a coupler to a NEMA 15 stepper motor which allows the sample to be strained at a rate of 0.75 microns per step pulse. A loading arm, to which the moving sample plate is affixed, transfers the rotational energy of the shaft to the translational motion of the tensile test by sliding atop an E-1 Ball Slide.

The test is performed by first placing a single ligament sample across the divide separating the two sample plates. A sealing wax is then soldered to the ligaments in order to rigidly affix the ligament to the sample plate after which the sample is now ready to be tested. The dimensions of the ligaments are obtained through the use of a Diagnostic Instruments 11.2 Color Mosaic digital camera connected to an Olympus BX-41 light microscope under 5X magnification. The test, recorded as a live video by the digital camera, is then performed as the ligament is strained at a rate 1 micron per second until failure occurs.

Due to the ligament's small size, approximately 90 microns in diameter and 1.9 mm in length, 20 successful tests of each type of ligament were performed in order to obtain a large statistical sampling. A successful test was defined as one in which two events occurred: first, a fracture had to be witnessed in the recorded video and second, the data indicated a stress peak indicating failure due to the testing load as opposed to failure as a result of stresses induced in mounting of the sample.

3.0 Results

Any composite material, whether it be nano or otherwise, performs on a level commiserate with both that of the matrix and filler as well as the interface between these entities [13]. Testing, therefore, of any composite examines the capability of each of these distinct components. Accordingly, the strength data here can then be correlated directly to both the strength of the added nanofibers themselves as well as to the interface between these nanofibers and the mesophase pitch matrix.

Applied Science Incorporated produces the Pyrograf III type nanofibers used in this study [85]. As can be seen in Table 4.1, each of the different types of nanofibers, PS, LHT, and HHT, are each modified to produce a slightly different nanofiber surface and structure. These differences in nanofiber structure were seen to directly relate to the performance of the carbon-carbon nanocomposite as is seen in the following analysis.

Table 4.1 Characteristics of carbon nanofiber [85]

		<i>Dispersive Surface Energy</i>	<i>Iron Content</i>
PR-19-PS	Pyrolitically stripped	40 (mj/m ²)	3.8%
PR-19-LHT	Graphitized fiber	40 (mj/m ²)	3.6 %
PR-19-HHT	Iron seed free graphitized fiber	36 (mj/m ²)	<100 ppm

In order to fully understand the properties that make carbon nanofibers unique, both the microstructure and surface of nanofibers samples were characterized. The nanofibers consist of a variety of carbon configurations: helical, straight, nested, carbon blacks all of which are narrowly different in diameter and length (Figure 4.12). However two main configurations seem to be dominant within the nanoconstituents: nested and straight carbon nanofibers.

Within each of these different types of configuration, many of the processes of formation run parallel. Carbon at low temperatures exhibits only local molecular ordering yet during heat treatment the increase in temperature results in the aromatic molecules become stacked in a column structure. Further heat treatment causes these columns to coalesce forming a distorted, wavy structure [14]. Surpassing a temperature of 2500°C, the distorted graphene layers of carbon become flattened forming an aligned structure, and if graphitic will attain the minimum interlayer spacing between graphene layers.

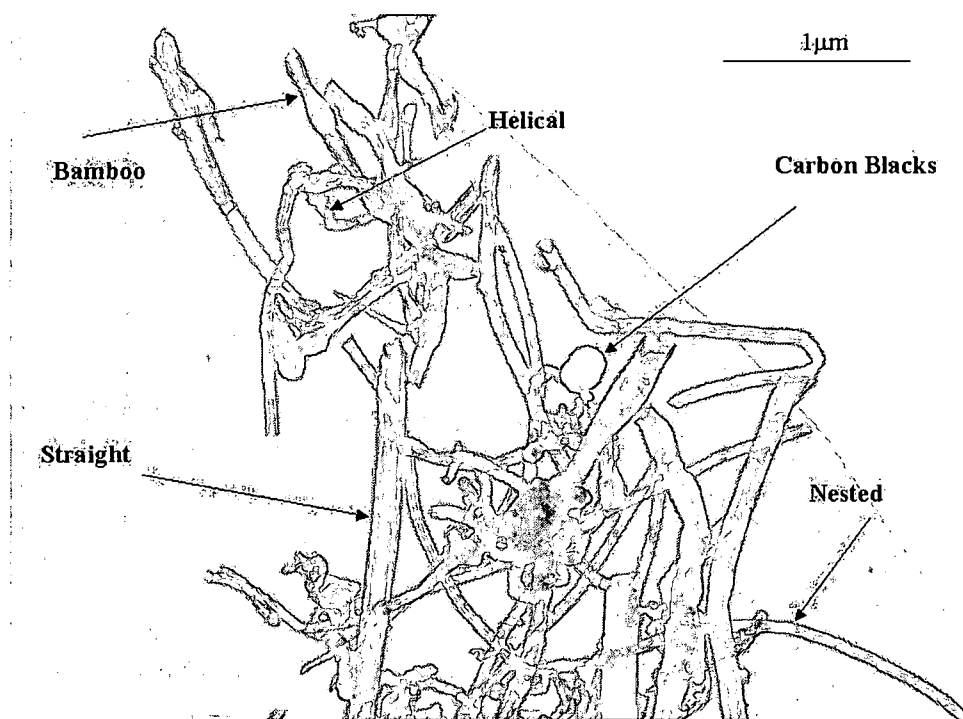


Fig. 4.12 Bright-field image of pristine carbon nanofibers (PS Fibers)

The fibers examined here all are believed to contain roughly the same distribution of carbon configurations. Yet due to differences in the heat treatment the perfection of these configurations varies as at low or no heat treatment the graphene layers will be spaced far apart limiting the strength of the nanofiber. Any discrepancies based on fiber type are a direct result of this fact and the remnant of the iron catalyst still present on the fibers.

3.1 Bulk Compression

As stated before, the bulk strength of carbon foam has been predicted to be most dependent upon the transverse shear strength at the midpoint of the foam's ligaments [94]. Consequently, any effort to enhance the mechanical performance of carbon foam must be centered upon the optimization of this strength. Currently, studies on enhancing ligament strength have focused

largely on processing improvements, although reinforcement has been suggested but until now not studied [84]. Consequently, this study focuses on evaluating the potential of reinforcement through a mechanical characterization of foams complimented with carbon nanofiber (CNF).

The reinforced carbon foams tested here were found to have strengths on the order of 1-2 MPa, values corresponding closely to other reports in literature [4,8,23,24,76,79,114]. Secondly, the specific strength and stiffness of the foams compared closely as well averaging about 4.5 MPa and 0.4 GPA, respectively. Most importantly, however, a keen dependence was found with respect to the strength of the foam and the type of carbon nanofiber employed indicating that performance could be greatly increased if both the reinforcement itself and its pre-foaming processing were optimized.

The processing dependence is readily apparent in the divergent behaviors of foams with reinforcements thoroughly dispersed in the pitch precursor versus those that were processed with incorporation of nanoconstituents "as produced". As seen in figure 4.13, the strength in the mixed foams increased with a rise in amount of CNF, a trend which also held true for the performance in stiffness. This trend was exactly the opposite, however, in the non-dispersed foams.

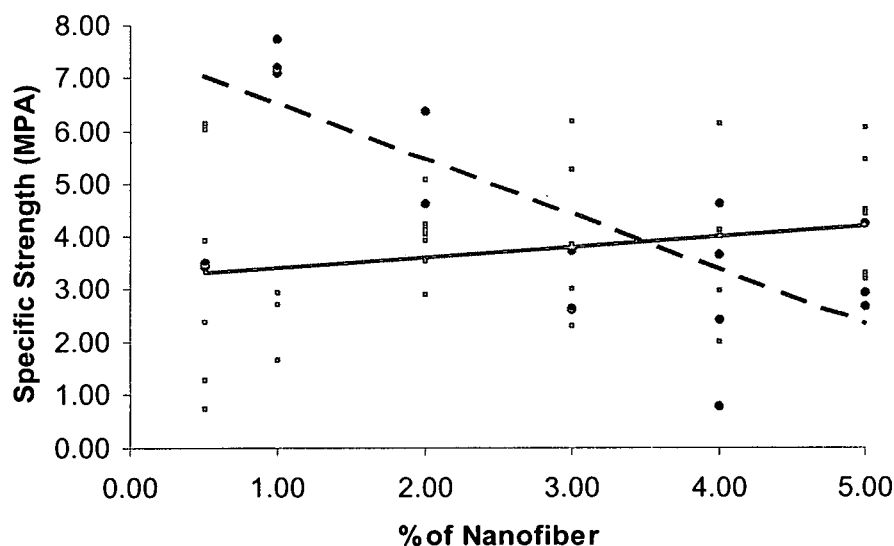


Fig. 4.13 Effect of shear mixing on foam strength (solid line corresponds to shear mixed samples)

Upon looking at figure 4.13 two trends are immediately obvious. First, when only small percentage by weight of nanoconstituent is added, 1 or 2 %, the non-dispersed reinforcements are actually stronger and stiffer than their dispersed counterparts. This is most likely due to the fact that at lower weight percentages there was a reduced probability for large agglomerates that could reduce performance. In addition, the small conglomerates that are present actually serve to pin cracks thus strengthening the material on the whole. At higher weight percentages of nanofiber, the likelihood of large agglomerates, clusters which are known to reduce the performance of the composite, greatly increases and consequently performance reduces as is seen in the great drop off of performance of the non-dispersed nanofibers [97,104]. Contrarily, when dispersed, the nanofiber reinforcement actually improves performance of the total foam indicating the strengthening capabilities of the carbon nanofibers.

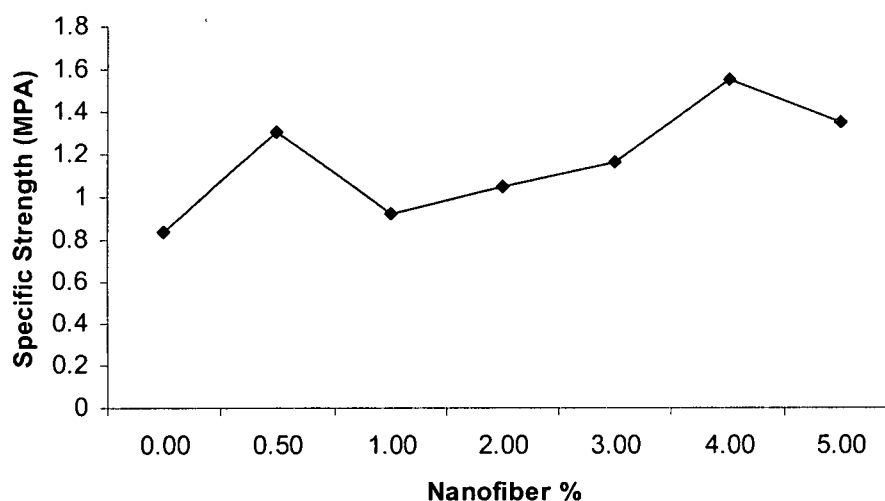


Fig. 4.14 Average specific strength increasing with nanofiber

This fact is seen in figure 4.14 as strength is seen to increase with additional amount of nanofiber in the matrix regardless of type. This indicates that the addition of a nanophase itself increases the performance of the carbon foam. It is likely that this is due to the reduction in shear plane size as a result of the nanofiber addition, a fact which will be explained in more detail later in this chapter.

Additionally, the type of nanofiber affects the performance as the nanofiber's structure will affect the ability of the nanofiber to strengthen the foam. Figures 4.15 and 4.16 show the drastic differences in both strength and stiffness of the foams with different types of nanofibers. This is to be expected as both the nanofiber and interface strength, two components which greatly determine the strength of the composite, depend upon the exact structure of the CNF [77].

The CNF's employed in this study greatly varied in terms of purity and structure. The PR-19-HHT nanofiber is highly heat treated with minimal

interlayer spacing without any remnant of catalyst, while on the other hand, the PR-19-PS nanofiber has larger interlayer spacing and residual amounts of catalyst [85]. Consequently, it is of no surprise that the HHT nanocomposite greatly outperformed the other nanofibers. Devoid of most defects, the HHT composites were able to form the best interfaces along with shouldering the greatest stress thus resulting in a higher performing nanocomposite. This effect was maximized as the amount of nanofibers in the composite was increased. It should also be noted that performance between the LHT and PS nanofiber was largely the same indicating similar structures and bonding capabilities between the two.

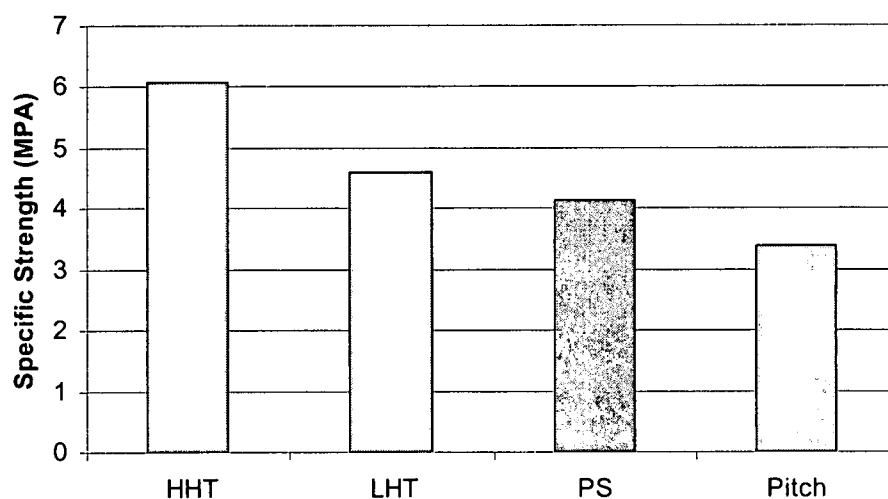


Fig. 4.15 Bulk specific strength of foams

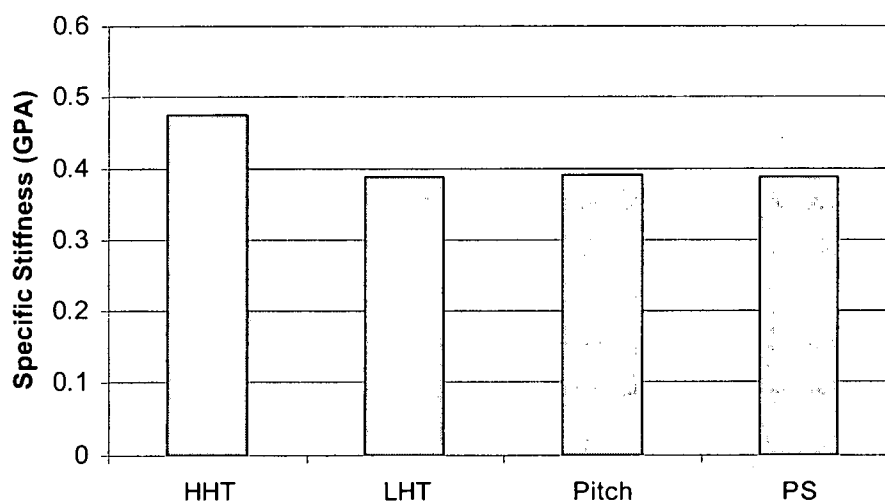


Fig. 4.16 Bulk specific stiffness of foams

3.2 Ligament Tensile Tests

As can be seen in the figure 4.17 and 4.18, ligament performance increased with an associated increase in heat treatment of the added carbon nanofibers in much the same fashion as the bulk tests. The ligaments containing HHT nanofiber, which due to its high heat treatment temperature most nearly resembles a perfect graphitic structure, had strengths of 1.3 times and 2.74 times that of the LHT and PS enhanced ligaments, respectively. Furthermore, each of the composites displayed both strengths and stiffnesses significantly greater than the unreinforced carbon foam ligaments thus indicating again that bulk carbon foams could be significantly improved with the adoption of carbon nanofiber fillers.

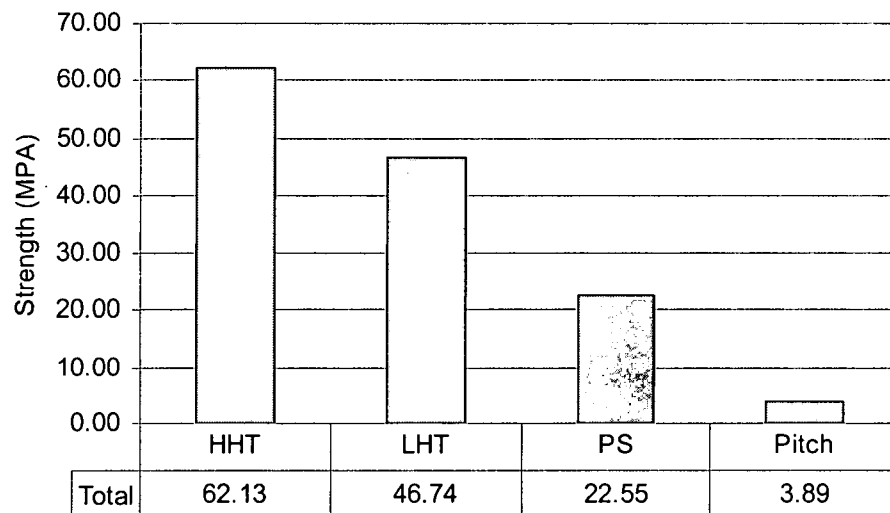


Fig. 4.17 Ligament strength

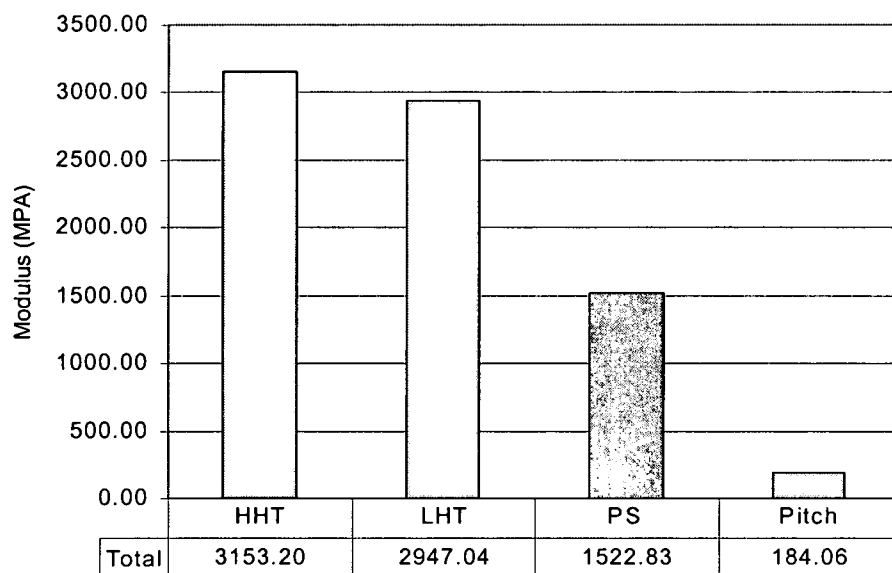


Fig. 4.18 Ligament stiffness

The increase in both strength and stiffness of the foam ligaments is most obviously due to the high strength of the nanofibers themselves, which have been reported to exhibit strengths and stiffnesses on the order of 12 and 600 MPa, respectively [77]. These high strengths do not transfer, however, if a suitable interface is not present since these first few atomic layers are most significant to the mechanical properties of any composite [81,117]. With this

in mind, it is of no surprise that the HHT enhanced ligaments showed the highest capability as they have the lowest defect density as their catalyst remnants have been removed during heat treatment.

An additional strengthening mechanism is the shape of the ligament itself. Since the foam ligament's matrix is composed of a carbon fiber precursor, mesophase pitch, the final strength of the ligament is directly dependent upon the degree of alignment which the graphitic crystallites attain during processing [13]. In a carbon foam, this alignment is maximized as the ligaments are continually strained during processing [34]. Furthermore in a nanocomposite, the material's capability will reach its acme as the strengthening phase becomes aligned to the direction of the applied force. Jin et al. showed that this type of alignment could be obtained in carbon nanotube composites through a mechanical stretching of the composite, a type of stretching which occurs intrinsically in carbon foam processing [37]. The effect of aspect ratio, the length of the ligament divided by the diameter of the ligament, which is a measure of the degree of strain encountered by the ligament during processing, is easily seen as shown in figures 4.19 and 4.20. For each type of ligament, regardless of type, on average as the ligament's aspect ratio increased so too did both the strength and stiffness.

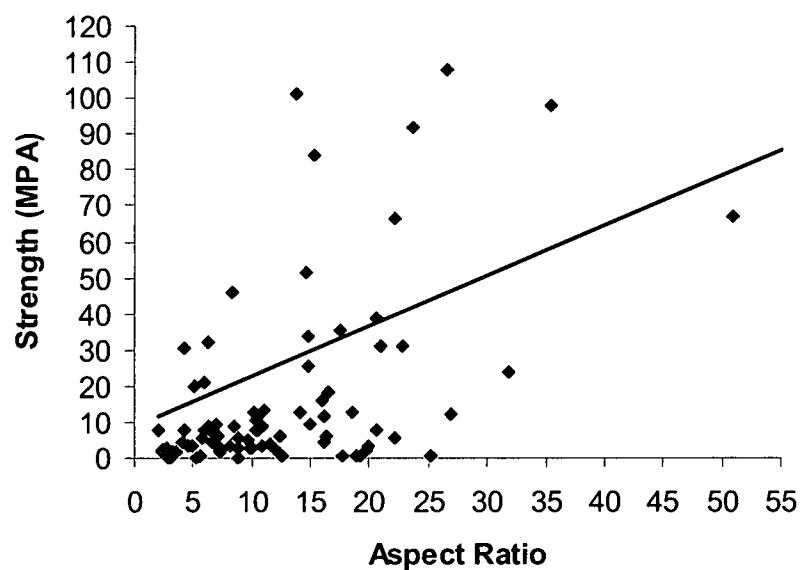


Fig. 4.19 Ligament strength increases with increasing aspect ratio

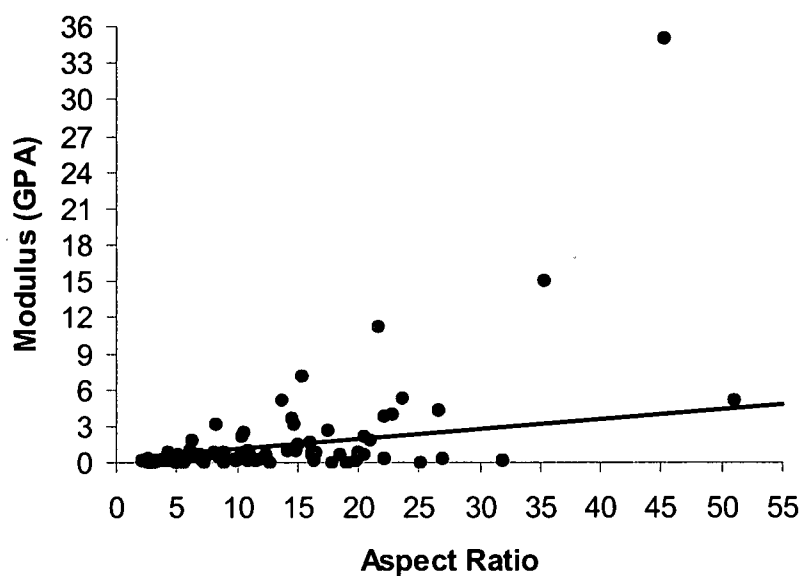


Fig. 4.20 Increasing modulus as aspect ratio increases

Therefore to truly judge the effect of each type of nanofiber the average aspect ratio through all the tests should be approximately equivalent to

mitigate any unequal strain strengthening effects. Consequently in this analysis an examination of the strength and modulus normalized with respect to the aspect ratio was performed. Figures 4.21 and 4.22 show the average normalized strength and moduli for each of the different types of nanofiber. Examining the normalized functioning of the ligaments, it becomes apparent that the PR-19-HHT enhanced ligaments do not outperform the other ligaments to the same extent as when only strength or stiffness is considered. This is due to the fact that the average aspect ratio of the HHT enhanced ligaments is greater than the associated average aspect ratio of the other types of tested ligaments. Yet when the normalized, strength and moduli are multiplied by the

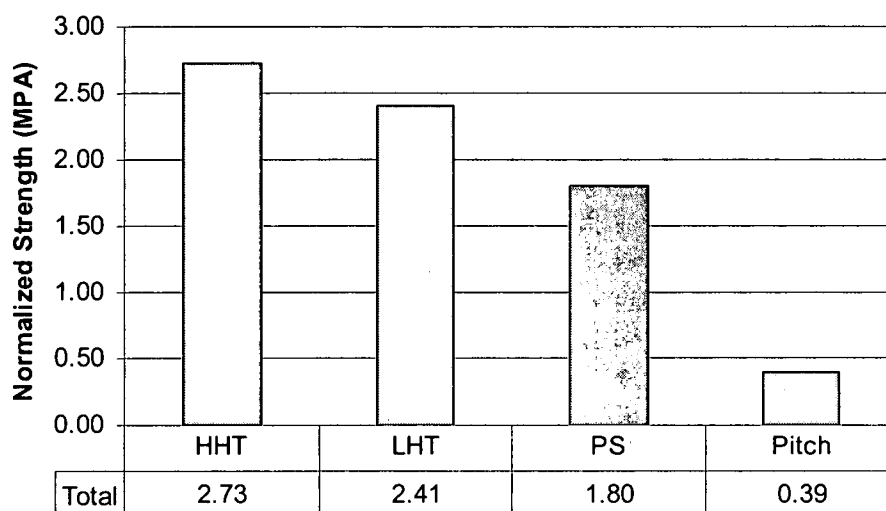


Fig. 4.21 Normalized ligament strength

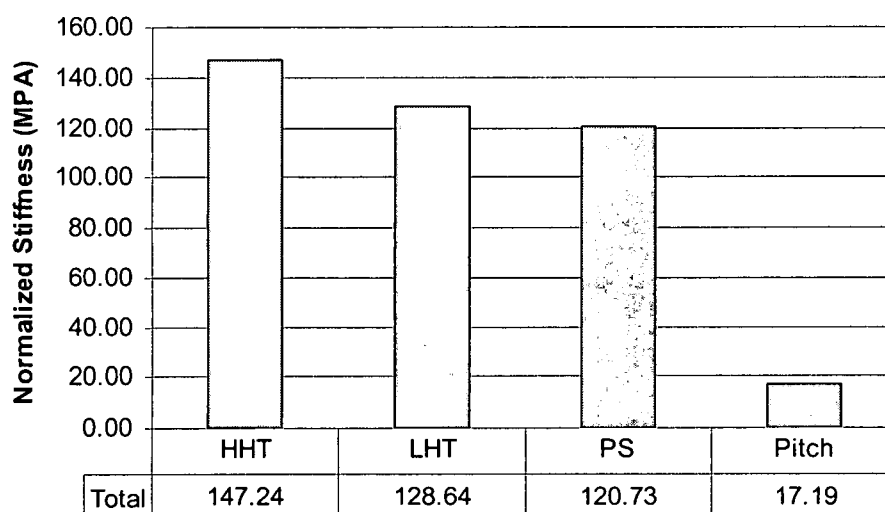


Fig. 4.22 Normalized ligament modulus

differences in average aspect ratio, the extent to which the HHT ligaments outperform becomes very similar to plain strength and stiffness measures. This fact further indicates that both the strengthening phase and the physical shape of the ligament play a role in the mechanical properties of the ligaments and hence the foam.

In the past carbon foam has been modeled as a series of P-100 carbon foam fibers connected together to form a three-dimensional graphitic network thus assuming that the ligaments themselves were composed of similar microstructure and shape to that of individual carbon fibers [33,34,94,95]. Furthermore, although in subsequent work the ligaments have been modeled to have both varying cross section and properties along the ligament, failure has continually been proposed to occur due to beam bending [94,25]. The strengths proposed herein, however, fall below the assumed ligament

strength of the models, a fact which was expected due to the discussion of section 1.1 in this chapter. It is believed that the video recording of the fracture gives insight into this apparent contradiction of data.

Carbon fiber has a unique microstructure of radially interlocked graphitic planes [13]. These interlocking planes give the fibers both their high strength and stiffness resulting in carbon fiber fracture being a highly brittle event. Consequently, from the previous modeling works it would be expected that the ligaments would fail in a similar brittle manner. As seen in figure 4.23, this is not the case as the majority of non-reinforced ligament failures occurred with some degree of peeling shear deformation during fracture. This type of fracture results in diminished strength and stiffness of the ligament with respect to the fiber assumption and indicates that the failure more likely occurs in a manner similar to a thin film or plate rather than a beam. Furthermore, it indicates that the molecular orientation of the ligament's graphene planes do not interlock as they do in standard carbon fibers.

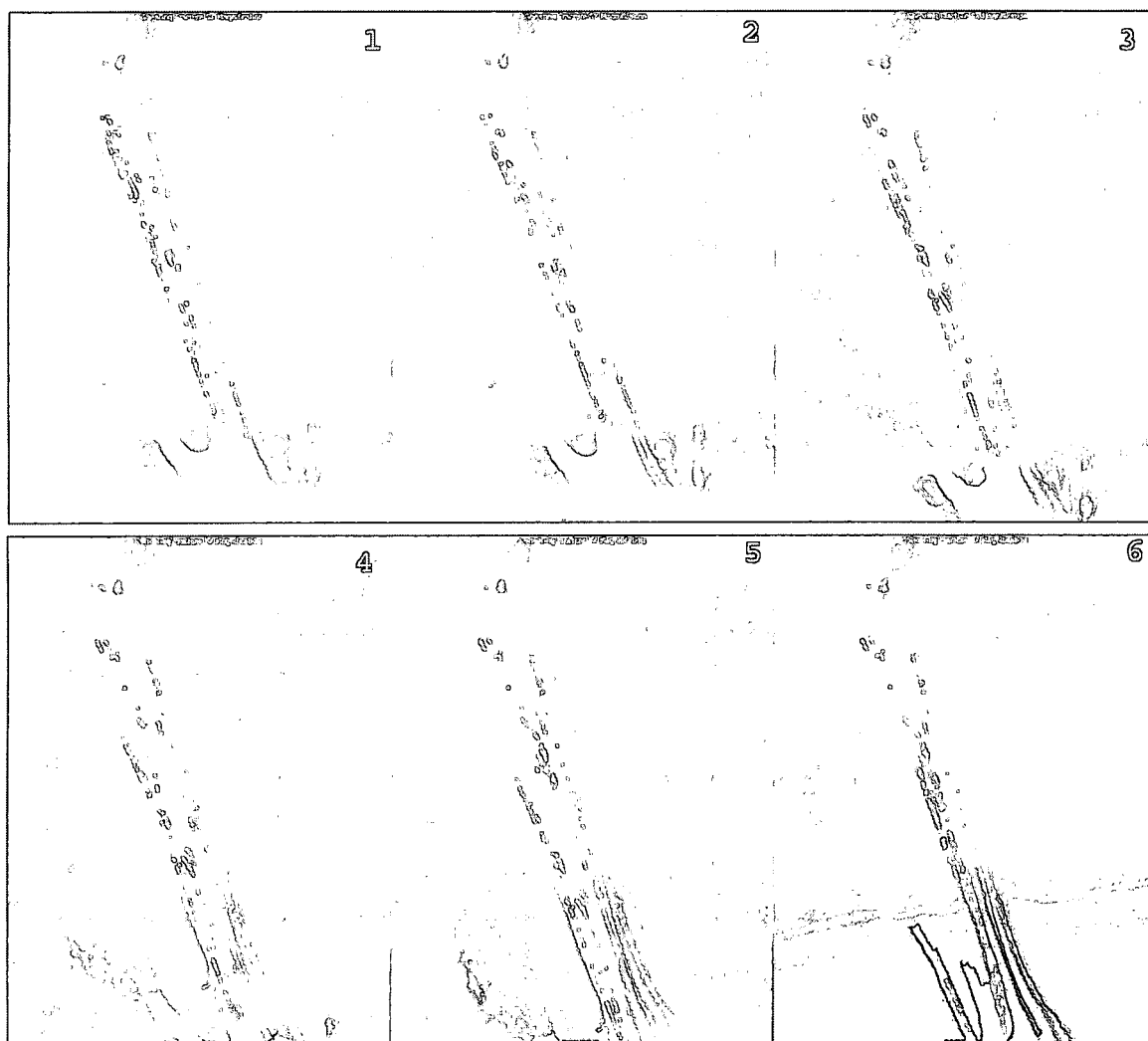


Fig. 4.23 Shearing failure characteristic of most ligament fractures

3.3 Discussion

In both the single ligament testing as well as that of the bulk, it was shown that addition of carbon nanofiber to the mesophase pitch matrix resulted in an increase in mechanical performance. Furthermore, the type of nanofiber introduced to the matrix determined the magnitude of this increase. In single ligament tests, the difference in capability between differing types of nanofiber was extremely large with HHT doped nanofibers outperforming purely pitch

ligaments by almost 20 times. This difference was not seen to be as large, however, with respect to the bulk testing as HHT foams outperformed pitch foams by only twice as much.

From these results it can be deduced that the effect of carbon nanofibers is mitigated in the bulk cellular material. This is due first to the fact that in a bulk foam, ligaments are oriented in a near random order. Consequently, several ligaments are loaded in a complex fashion. Hence, the nanofiber's effect is reduced since the loading occurs in a direction in which the nanofiber is not aligned. Secondly, in a ligamentary test only the ligament itself is being tested whereas in a bulk test the junction between ligaments is tested as well. In the region of the junction, high concentrations of disclinations occur allowing for the connection of ligaments entering at different angles. In these folds, the distances between basal planes of carbon are maximized. With the addition of nanofibers, the distances between these planes are extended even further and the junctions are further weakened thus limiting the aid of the nanofiber in the ligament region of the foam.

The strengthening that does occur is a direct result of not only the natural high strength of the CNF but also the modification of the foam microstructure itself. Shown in figure 4.24 it can be seen the great decrease in molecular orientation of the nanofiber enhanced carbon foams. This decrease indicates that the nanofibers serve as a crosslinker limiting the growth of graphene layers. In crosslinking, the fibers enhance the lateral strength between graphene layers while at the same time promoting a more granular

microstructure more similar to that of carbon fibers as shown in the series of pictures in figure 4.25.



Fig. 4.24 a: Pitch based foam with large molecular orientation
b: Effect of CNF on molecular orientation (40X)

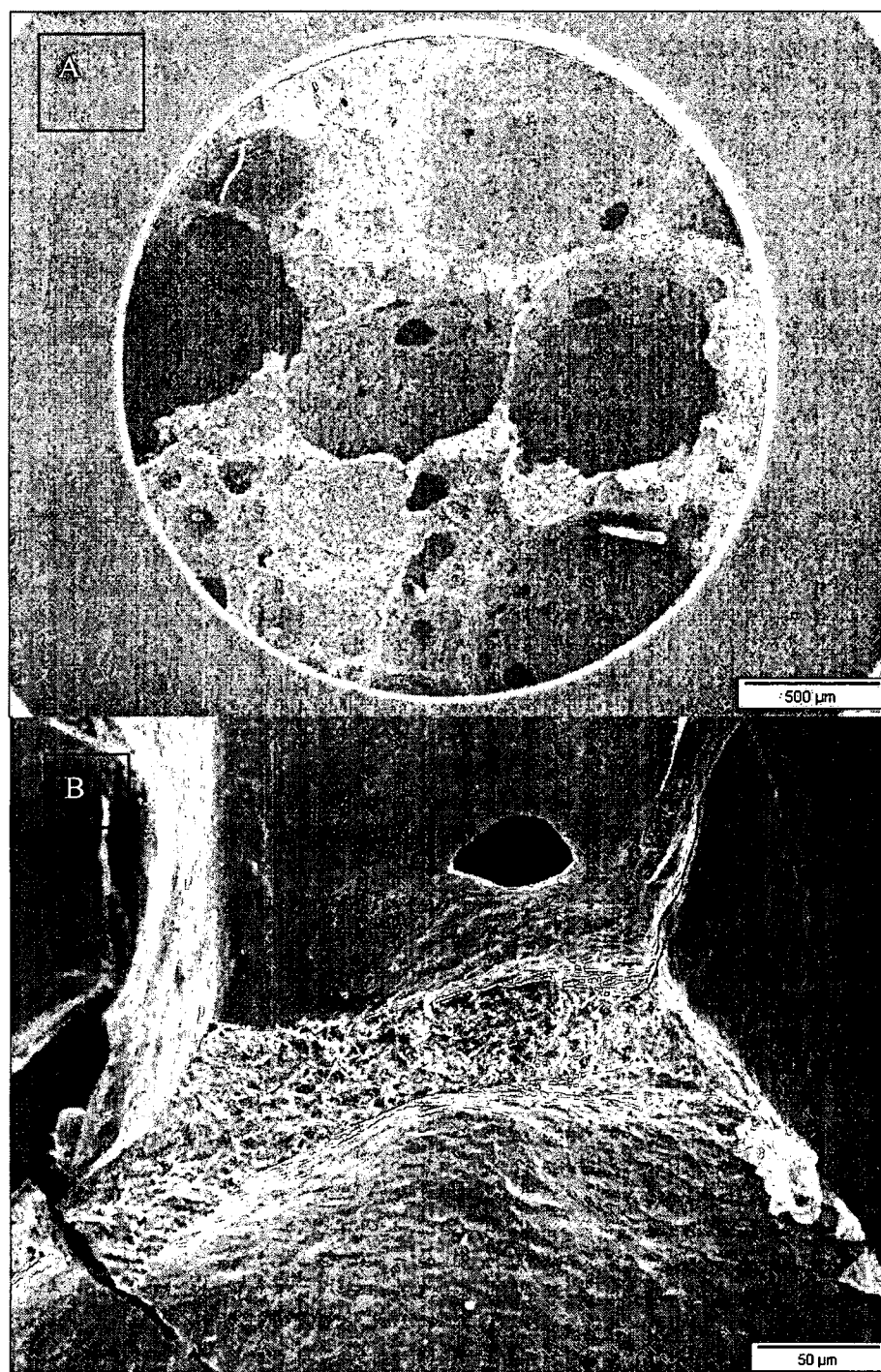


Fig 4.25 Granular microstructure of CNF enhanced carbon foams

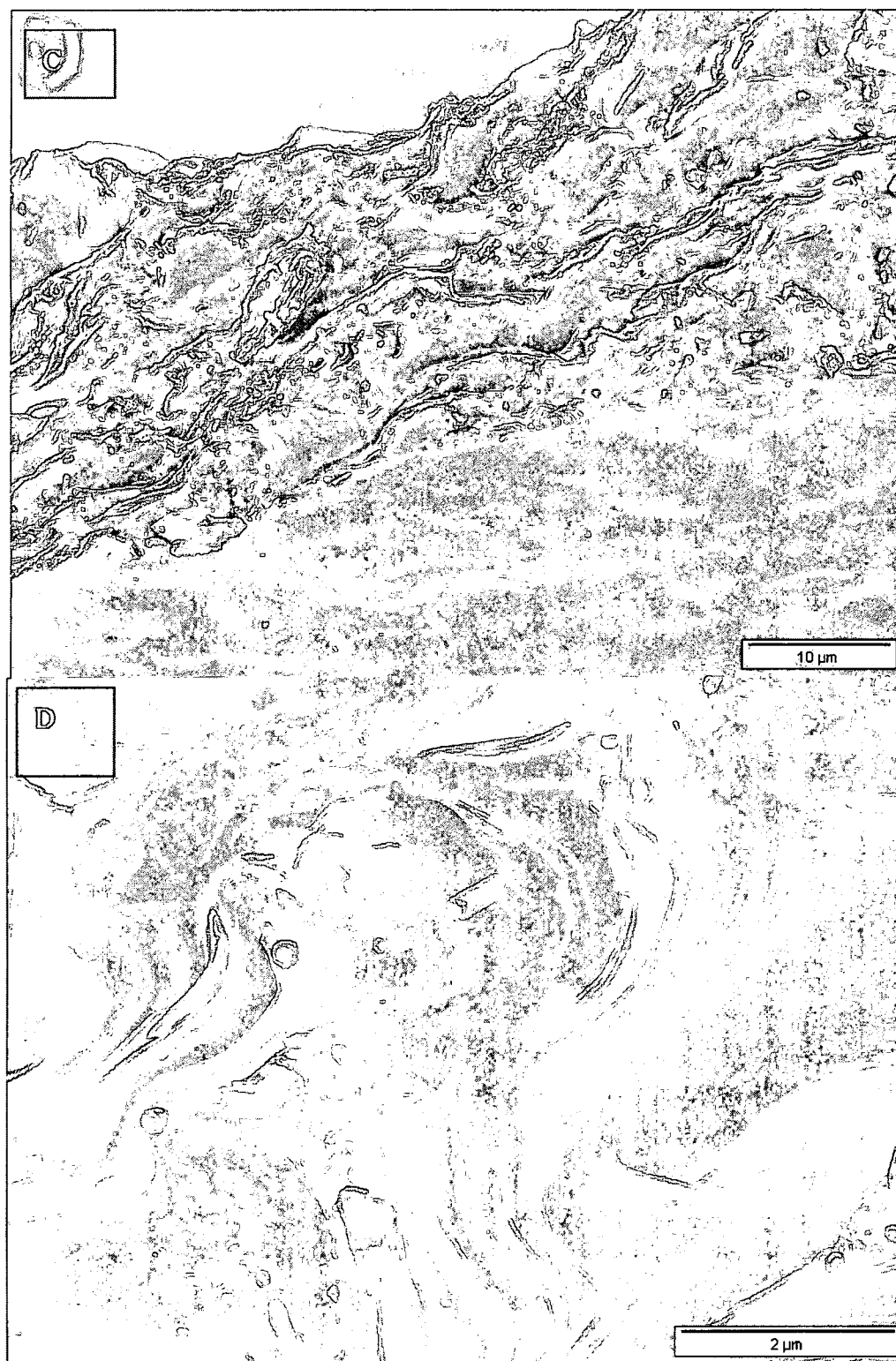


Fig 4.25 (c & d) Granular microstructure of CNF enhanced carbon foams ctd.

4.0 Conclusions

A series of carbon foams were produced with the addition of differing types of carbon nanofibers. From these foams two types of mechanical tests were performed to gain insight into both the effect of carbon nanofibers on the performance of carbon foams as well as to understand the failure mechanism behind fracture of carbon foams. The testing both of the bulk and single ligaments indicated that with addition of carbon nanofibers to the foam mechanical capability increased. The amount of increase was directly dependent upon both the amount and type of nanofiber utilized as CNF's with higher heat treatments resulted in foams of higher performance. This increase in performance is the result both of the actual strengthening of the CNF's themselves as well as the more granular structure which occurs as a result of the implementation of nanofiber into the foam.

Chapter 5

Bubble Size Distribution of Nanofiber Doped Carbon Foams

1.0 Introduction

As with any material, the capability of carbon foam is dependent on the characteristics of its microstructure. Unlike other materials, however, the microstructure of the foam is completely dependent upon the growth and intersection of a myriad of bubbles during processing. Consequently, the extent and uniformity with which bubbles grow during carbon foam processing plays a significant role in the final physical properties of the material.

Researchers have long been cognizant of this aspect of foam performance, as several studies have linked the porosity, and as such indirectly the bubble size, to the mechanical strength and stiffness of the foam [25, 94]. In much the same way, all modeling works in the subject have had at their heart an assumption with respect to the porosity, i.e. bubble size, of the foam before any computation could occur [24,34, 94,111,112,]. Yet in each of these different studies all conclusions were based on the assumption that this prescribed bubble size was consistent throughout the entire foam. In

practice, however, bubble size is rarely completely uniform as can be seen in a typical micrograph of carbon foam shown in Figure 5.1 [17].



Fig. 5.1 Non-uniformity of bubble size in carbon foam

These areas of non-uniform bubble size are deleterious as they create stress concentrations, and thus degraded mechanical performance, as well as regions of reduced thermal capability as well. Therefore, in the study of foams, it is as important to investigate the distribution of bubble sizes in a sample as it is to examine the bubble size itself. Researchers of carbon foam have largely neglected this aspect of foam processing as few studies have even examined the parameters affecting bubble size with an even smaller percentage including the distribution of these sizes in the analysis.

In 1998, Kearns et al. examined the effects of different blowing agents, along with temperature and pressure on the final bubble size in carbon foams [41]. In their analysis, it was found that increasing the foaming temperature and pressure while decreasing the molecular size of the blowing agent resulted in foams with increased cell size [41]. A separate study performed in 2000 by researchers at Oak Ridge National Labs found similar

relations with respect to temperature in a non-thermodynamic flash foaming technique [50]. These studies, however, all fail to quantify the bubble size distribution in their analysis.

This study undertakes measuring the bubble size distribution in a series of carbon foams using techniques previously utilized in the analysis of other types of foam materials. Processing parameters such as temperature and pressure affecting both the bubble size and distribution will be analyzed. In addition, the effect of nanoadditives on the foam microstructure will be examined in order to determine how their addition impacts both bubble size and distribution.

2.0 Experimental Method

Foams of different nanofiber type and amount were processed using a thermodynamic flash technique as described in chapter 1. Foaming temperature and pressure were set to 275°C and 1000 psi respectively yet fluctuations on the order of 10°C and 25 psi occurred. After foaming, a representative portion of the foam was mechanically extracted at which point it was then vacuum impregnated with epoxy. After impregnation, the sample was then polished and placed under a light microscope where a series of micrographs were obtained describing a representative cross section of the foam.

Using image analysis software, data was then obtained relating the size of each bubble in the cross section [17,50]. From this information a series of relations could be made for each sample with respect both to average bubble

size as well as bubble size distribution. Average bubble size was calculated using both a number average technique where each bubble contributes to the average equally along with a volume average technique in which larger bubbles contribute more heavily. The volume average was included in this study in order more easily recognize conditions leading to the growth of a few anomalously large bubbles. The equations describing the number and volume average are given in equations 1 and 2, respectively [17].

$$\frac{1}{n} \sum_{i=1}^n r_i \quad (1)$$

$$\frac{1}{n} \left(\sum_{i=1}^n r_i^3 \right)^{1/3} \quad (2)$$

From these averages it is then possible to obtain a measurement which gives insight into the bubble size distribution. Since foaming frequently results in an abnormal distribution of data, a consequence of a few large bubbles, the standard deviation is not the optimal parameter with which to measure the bubble distribution. Rather, the skewness number, S_k , is more able to accurately describe the bubble distribution where a larger value corresponds to a large distribution of the data set [17]. The dimensionless skewness number, shown in equation 3, was calculated using both the number and volume average.

$$S_k = \frac{\left(\frac{1}{n} \sum_{i=1}^n (r_i - r_{avg})^3 \right)}{\left(\frac{1}{(n-1)} \sum_{i=1}^n (r_i - r_{avg})^2 \right)^{3/2}} \quad (3)$$

From these calculations, both the bubble size and bubble size distribution could be calculated for each of the different processing parameters as well as the different material compositions.

3.0 Results and Discussion

Previous studies of basic carbon foams have shown that under all processing conditions an increase in the foaming temperature results in an associated increase in the average bubble size [50, 41]. Figure 5.2 further substantiates this fact as similar trends for bubble radius were found for foams enhanced with carbon nanofibers. Additionally, it was found that the distributions in bubble size, as indicated by a higher skewness number, increased as well with higher processing temperatures as is seen figure 5.3. It should be noted the acute dependence with which bubble size and BSD rely on temperature as the following data shows the significant differences in microstructure resulting from only a 15°C change in temperature. Contrarily, the small fluctuations in pressure which occurred resulted in only slight changes in the average bubble size and BSD.

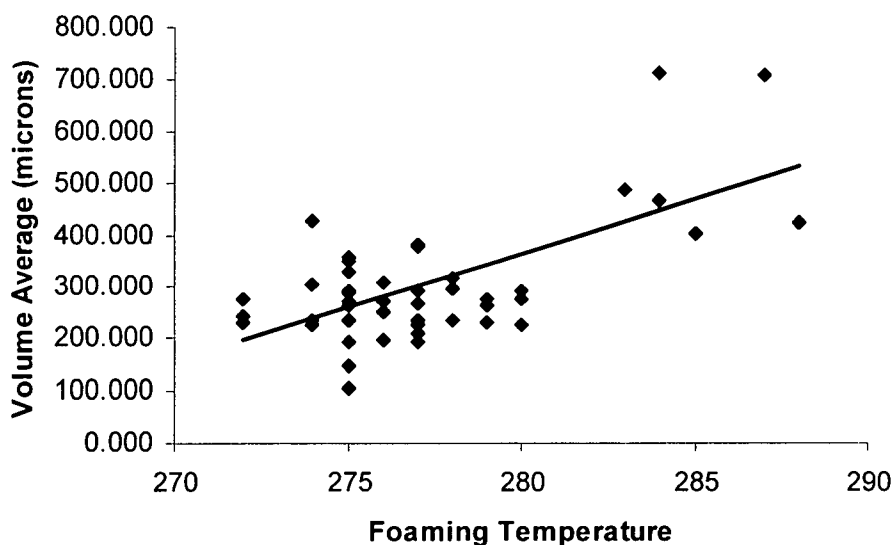


Fig. 5.2 Increasing average bubble size with temperature

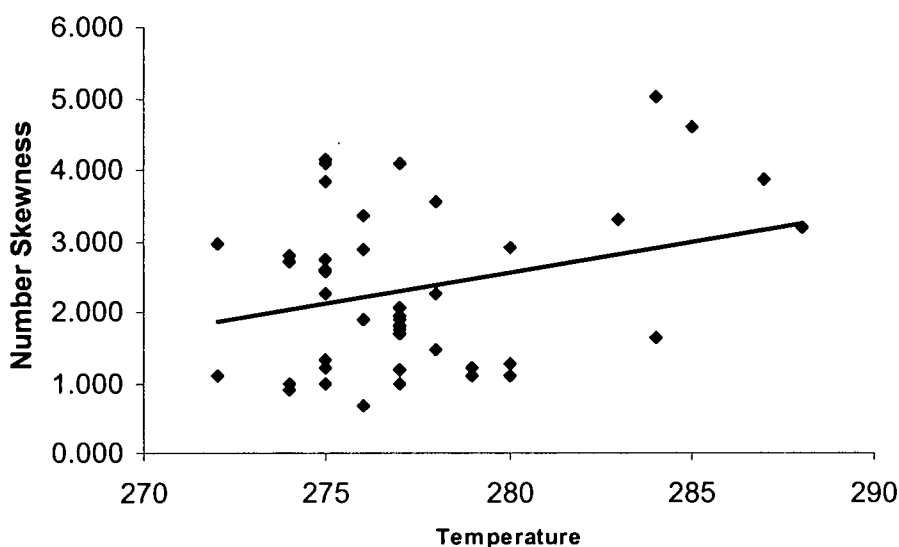


Fig. 5.3 Increasing bubble distribution with temperature

Bubbles tend to grow larger at higher temperatures due in large part to the associated lower viscosities present at these conditions. As a result of the lower viscosities, the bubbles have a longer growth time which results in a larger final size. A thorough explanation of this effect can be found in chapter 2. The extended growth periods affect the bubble distribution as well due to

the large amount of heterogeneous nucleation taking place across a finite time range [10,11]. Consequently, as the growth time increases so too does the size disparity between bubbles which nucleated at different times.

The shape and uniformity of the microstructure was affected as well by the degree to which a strengthening phase was added to the mesophase pitch matrix. Adding increasing amounts of nanofibers to the pitch precursor lead to a direct increase in the volume average of the bubble radius as is seen in figure 5.4. This trend, however, is not as distinctly apparent when the average bubble radius is computed using a number average technique. These facts when coupled together indicate that as the percentage of added nanofibers increases so too does the likelihood for a few anomalously large bubbles to be present in the foam. Consequently, it is of no surprise that the volume average skewness number increases as well with larger percentages of strengthening phase thus indicating a larger distribution of bubble sizes as is seen in figure 5.5.

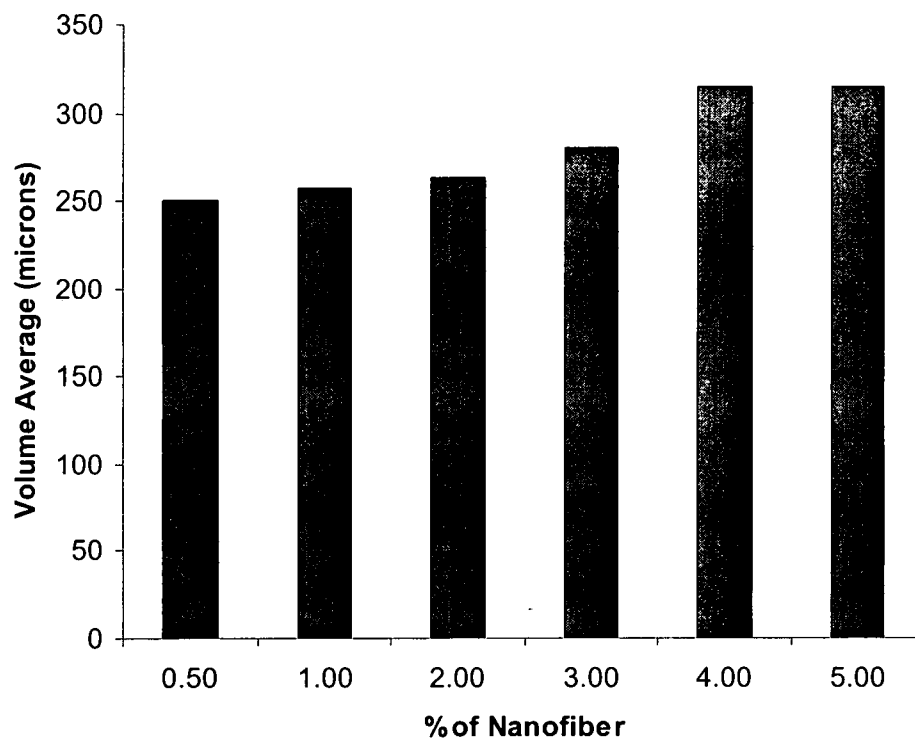


Fig. 5.4 Increasing average volume size and nanofiber

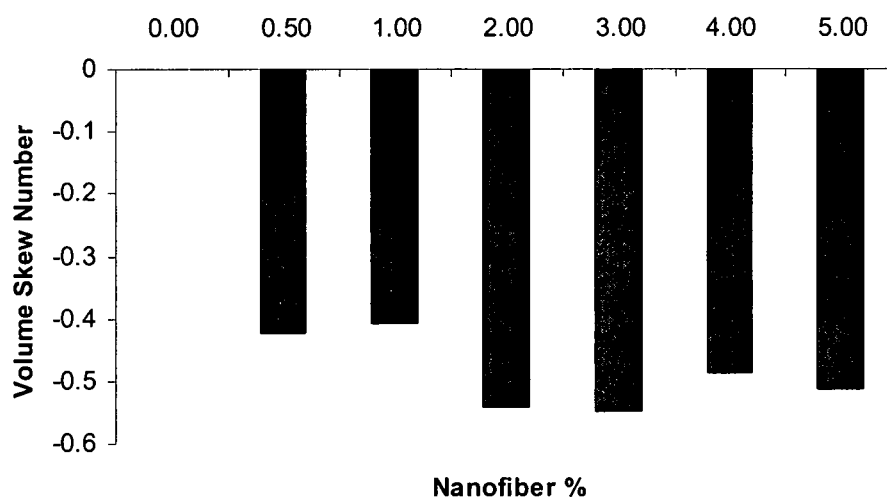


Fig. 5.5 Increasing BSD with nanofiber percentage

Since nucleation density is inversely dependent upon the surface tension of the liquid melt, it is readily apparent that an increase in one parameter would lead to a decrease in the other [10,11,89]. In this case, addition of the nanoconstituent leads to an increase in surface tension of the liquid melt and hence to a smaller nucleation density. With less nucleation, bubbles are allowed to grow larger as the same amount of gas is available for a fewer amount of expanding bubbles.

The larger distributions associated with increased amounts of nanofiber indicate that the strengthening phase is not uniformly dispersed throughout the pitch matrix. Rather, it is believed that hot zones of nanofiber aggregates are present during the foaming, a phenomenon which severely limits the growth of any bubbles in their vicinity. This results in extremely limited growth in the regions close to nanofiber conglomerates with bubbles outside of these zones growing substantially bigger thus resulting in a significant range of bubble size distribution.

While the quantity of fiber plays a significant role in both the size and distribution of bubble sizes in the foam, the data suggests that the type of fiber plays a very limited role in the determination of bubble microstructure. It was found that foams made with the addition of PR-19-HHT fiber when contrasted with foams containing PR-19-LHT fiber had an average radius within 1% of one another while the PS foams had averages that differed from the other foams by only 10%. Furthermore, the skewness numbers for each

different type of foam were all within 11% of one another thus indicating that while the fibers themselves play a role in microstructure development the type of fiber has little effect.

4.0 *Conclusions*

Although the importance of average bubble size has long been recognized by researchers an associated parameter, bubble size distribution, has largely been ignored in past studies. Large distributions in the bubble size of a foam, however, can play a significant role in performance and hence were studied here. It was determined that foaming temperature plays a large role both in determining the average bubble size as well as the distribution of these sizes with increases in temperature resulting in an increase in both parameters. Similarly the amount of nanofiber, regardless of type, was found to increase both parameters as well, though with not with the same acute effect as temperature. Future studies should seek to relate the dispersion of the nanospecies within the matrix to bubble size distribution. Currently, aggregates of nanofibers are believed to cause the distribution in bubble size, a problem which must be solved before the advantages of nanofibers can fully be implemented in the making of carbon foam. In addition, the effect of surface functionalization on the nanofibers themselves should be examined to determine their effect on microstructural development.

Chapter 6

The Process Property Link

A host of conclusions is readily available with respect to the series of experiments performed within this study with value both to the realm of carbon-carbon nanocomposites as well to the realm of cellular materials. The true value of the current study, however, lies in its ability to produce a link between the processing of carbon foams and their performance. To establish this link, information from each part of the current study must be synthesized. The following then is a synthesis of each of the seemingly eclectic studies joined in this thesis.

It was shown in chapter 4 that the aspect ratio of a ligament had a distinct effect on the mechanical performance. For example, among ligaments having equivalent normalized performance, that is strength and stiffness divided by aspect ratio, actual strength and stiffness could vary by over an order of magnitude. Furthermore, it was seen that qualitatively as the aspect ratio of a ligament increased so too on average did its load bearing capability.

This phenomenon is largely due to the degree of alignment which occurs during the formation of the microstructure of the foam during processing. As bubbles continue to impinge on one another the liquid film between them is strained to an ever-higher degree which causes the liquid crystals of the mesophase pitch to align along the axis of the ligament [32]. Furthermore, a similar phenomenon occurs in the molten liquid when nanofibers are present. As the liquid strains further, the fibers become more aligned along the axis of straining [37]. Consequently, it is true that the impact of aspect ratio is heightened when the pitch matrix is supplemented yet the phenomenon is present regardless. Hence, processing of the foams should seek to maximize this parameter of aspect ratio.

To maximize aspect ratio, bubble size must be maximized while simultaneously insuring uniformity throughout the foam to prevent stress concentrations. In the previous chapter, it was proffered that changes of several different parameters could result in an increase in average bubble size of the foam. Increases in initial bubble pressure, i.e. foaming pressure, along with a decrease in viscosity most directly enlarged the final average bubble size.

In conjunction with the conclusions obtained from the numerical model, information obtained from study of the nucleation can also be used to maximize average bubble size. Nucleation density is inversely proportional to final bubble size. Consequently, in order to maximize bubble size nucleation

density should be minimized. This density is highly dependent both on the viscosity of the molten liquid as well as the surface tension. A decrease in either one of these parameters leads directly to an increase in nucleation density. Therefore, to maximize final bubble size these parameters should be increased with measure as too big of an increase can lead to limited growth.

A problem arises, however, with increasing bubble radius. For although an increase in aspect ratio results in higher ligament properties, the associated reduction in density reduces the overall performance of the foam. Consequently, a strategy must be devised to increase the aspect ratio of the ligaments while at the same time conserving the overall density of the foam. Bubble shape is a novel parameter, uninvestigated until now, which can accomplish this feat.

In chapter 3, it was shown that if a foam is expanded in a non-symmetric pressure release bubble shape is highly affected. Furthermore, it was shown that the same parameters which influence final bubble size also play a large role in the shape that the bubble takes on under these non-symmetric expanding conditions. Most simply, parameters increasing final bubble size minimize non-spherical behavior. Pertinent to this discussion is the fact that with an increase in non-spherical behavior of the bubble is an associated increase in aspect ratio of the ligaments making up the two major axis of that bubble while density largely remains constant.

This non-spherical behavior can then be used to, on average, increase the ligaments aspect ratio along a certain direction giving increased performance

along that direction while at the same time minimizing the simultaneous decrease in overall density of the foam. Utilizing this strategy would lead to foams with an increase in specific properties along the critical direction of the foam. Consequently, through careful control of the foaming pressure, its release, along with viscosity and its rate of change, as well as surface tension, ligament aspect ratio can be maximized with minimal decreases in density. This strategy would result in tailorable foam with enhanced properties in a direction of the material designers discretion. Further enhancement is then obtainable through the use of nanofibers thoroughly dispersed prior to foaming with careful knowledge of the nanoconstituents effects on expansion and nucleation. Utilizing these improvements would lead to a foam composite of higher capability than that which is currently available.

One such objection to this strategy will likely be the loss of the foam's believed isotropic behavior. This belief, however, is largely false, as it has been shown that carbon foam is actually anisotropic with respect to the foaming direction [50]. This anisotropic behavior has not been heavily studied nor has it been exploited for its advantages in much the same manner as composites utilize their anisotropy. This strategy is one such exploitation.

Carbon foam's processing has largely been a black box to material designers. The suggestions offered in this thesis are one such strategy to link the processing with the properties of carbon foam. While this study by no

means has completed utilization of the strategy it is the author's belief that viability has been proven.

BIBLIOGRAPHY

- [1] Amon M, Denson C. Polymer Engineering and Science 1984;
24:1026-1034.
- [2] Anderson DP, Gunnison KE, Hager JW. Mat. Res. Soc. Sym. 1992;
270: 47-52.
- [3] Anderson DP, Wapner PG, Curliss DB. Mat. Res. Soc. Sym. 1992;
270: 59-64.
- [4] Anderson DP, Kearns KM, Klett JW, Roy AK. Aerospace Conference
Proceedings IEEE, Big Sky MT USA 2000; 4: 193-200.
- [5] Arefmanesh A, Advani S, Michaelides E. Inter. J. Ht. and Ms. Trans.
1992; 35: 1711-1722.
- [6] Barlow EJ, Langlois WE. IBM Research Journal 1962; 6: 329-337.
- [7] Beechem T, Elgafy A, Lafdi K. Carbon 2005; 43:1055-1064 .
- [8] Bunning TJ, Jeon HG, Roy AK, Kearns KM, Farmer BL, et. al. Journal
of Applied Polymer Science 2003; 87: 2348-2355.
- [9] Christensen RM. Mech. Phys. Solids 1986; 34: 563-578.
- [10] Colton JS, Suh NP. Polymer Engineering and Science 1987; 27: 485-
492.
- [11] Colton JS, Suh NP. Polymer Engineering and Science 1987; 27: 500-
503.

- [12] Coursey JS, Kim J, Roh H, Boudreaux PJ. IMECE 2002. New Orleans LA USA. 2002.
- [13] Donnet JB. Carbon Fibers, New York: Dekker, 1998.
- [14] Dutta D, Hill CS, Anderson DP. Mat. Res. Soc. Symp. 1994; 349: 61-66.
- [15] Dutta D, Hill CS. Cellular and microcellular materials. ASME 1994; 53: 63-70.
- [16] Electronic Design. April 3, 2000. 36.
- [17] Engelsen CW, Isarin JC, Gooijer H, Warmoeskerken MMCG, Wassink JG. Autex Research Journal 2002; 2: 14-27.
- [18] Fitzgerald DD, Taylor GH, Peennock GM. Carbon 1989; 32: 1389.
- [19] Fleurot O, Edie DD. J. of Rheology 1998; 42: 781-793.
- [20] Gaies D, Faber KT. Carbon 2002; 40: 1131-1150.
- [21] Gallego NC, Armstrong B, Mcmillan AD, Klett JW. Oak Ridge National Labs 2003 Progress Report. 23-28.
- [22] Gallego NC, Klett JW, Mcmillan AD. Intl. Conf. on Carbon Beijing, China; 2002.
- [23] Gallego NC, Klett JW. Carbon 2003; 41: 1441-1446.
- [24] Garman RW, Elwell RJ. PCIM Conference, Chicago IL USA. 2001.
- [25] Gibson LJ, Ashby MF. Cellular Solids: Structure and Properties, 2nd Edition. Cambridge University Press. UK.
- [26] Gong Qm, Zhi L, Li D, Bai Xd, Liang J. Solid State Communications 2004; 131: 399-404.

- [27] Googin J, Napier J. US Patent 3345440. 1967.
- [28] Gou Z, Wu KH, Klett J. 6th International Conf. on Composites Engineering. Orlando FL USA, July 1998.
- [29] Hager JW, Anderson DP. 21st Biennial Conference on Carbon, Buffalo NY USA; 1993: 102-103.
- [30] Hager JW, Lake ML. Mat. Res. Soc. Sym. 1992; 270: 29-33.
- [31] Hager JW. Mat. Res. Soc. Sym. 1992; 270: 41-46.
- [32] Hall R, Hager JW. 21st Biennial Conference on Carbon. Buffalo, NY; 1993: 100-101.
- [33] Hall RB, Hager JW. J. Composite Materials 1996; 30(17): 1922-1937.
- [34] Hall RB, Hager JW. Mat. Res. Soc. Symp. 1994; 349: 67-71.
- [35] Han CD, Yoo HJ. A.I.Ch.E Journal 1982; 28: 1002-1009.
- [36] Hara SK, Schowalter WR. J. of Non-Newtonian Fluid Mech. 1984; 14: 249-256.
- [37] Jin L, Bower C, Zhou O. Applied Physics Letters 1998; 73: 3842-3844.
- [38] Lafdi K, Bonnamy S, Oberlin A. Carbon 1992; 30: 533.
- [39] Lafdi K, Bonnamy S, Oberlin A. Carbon 1994; 32: 11.
- [40] Kearns K. Air Force Research Lab Technical Brief; ML-00-13. 2000.
- [41] Kearns KM, Anderson DP, Anderson HJ. Mat. Res. Soc. Symp. 1998; 521: 185-190.
- [42] Kearns KM. US Patent 5,868,974. 1999.
- [43] Kearns KM. US Patent 5,961,814. 1999.

- [44] Klett J, Conway, B. International SAMPE Symposium and Exhibition
2000; 45 1933-1.
- [45] Klett JW. US Patent 6,261,485, 2002.
- [46] Klett JW. US Patent 6,387,343, 2002.
- [47] Klett JW, Burchell TD. US Patent 6,037,032. 2000.
- [48] Klett JW. US Patent 6,287,375. 2001.
- [49] Klett JW, Gallego N, Burchell T, Bailey J. Proceedings of the 2nd World
Conf. on Carbon, Lexington KY USA, 2001.
- [50] Klett J, Hardy R, Romine E, Walls C, Burchell T. Carbon 2000; 38:
953-973.
- [51] Klett JW, Burchell TD. Eurocarbon 98: Science and Technology of
Carbon, Published French Carbon Group, Strasbourg, France, July
5-9, 1998.
- [52] Klett J, Jones S, Klett L, Walls C. SAMPE Sym. Long Beach California
USA, 2003.
- [53] Klett J, Mcmillan A, Ott R. Proc. Of Automotive Engineering
Government/Industry Meeting, Washington DC, June 19-21, 2000.
- [54] Klett JW. J. of Comp. in Man. 1998; 15: 1-7.
- [55] Klett JW, Klett L, Burchell T, Walls C. SAE 2000.
- [56] Klett JW. US Patent 6,033,506. 2000.
- [57] Klett JW, Klett L, Strizak J, Williams M, Mcmillan A, Valencia J,
Creeden T. 24th Annual Conference on Ceramic, Metal, and

Carbon Composites, Materials and Structures. Cocoa Beach FL
USA, January 2000.

- [58] Klett JW, Mcmillan A, Ott R. Society of Automotive Engineering
Government/Industry Meeting. Washington DC USA 2000.
- [59] Klett JW, McMillan AD, Gallego NC, Burchell TD, Walls CA. Carbon
2004; 42: 1849-1852.
- [60] Klett JW, Mcmillan AD, Gallego NC, Walls CA. Journal of Materials
Science 2004; 39: 3659-3676.
- [61] Klett JW, US Patent 6,398,994. 2002.
- [62] Klett J, Lowden R, McMillan A. Proceedings of the 2nd World
Conference on Carbon, Lexington KY USA, 2001.
- [63] Klett, JW. Proceedings of the 43rd International SAMPE Symposium,
May 31-June 4, Anaheim, California, SAMPE, 1998.
- [64] Klett, JW. US Patent 6,344,159. 2002.
- [65] Klett L, Klett JW. Proceedings of the 24th Bienial Conference on
Carbon, July 11-16, Charleston, SC, 1999: 310.
- [66] Klett JW, Tee C, Stinton DP, Yu NA. Proceedings of the 1st World
Conf. on Carbon, Berlin Germany 2000: 244.
- [67] Klett JW, Walls C, Burchell T. Int'l Conf. on Carbon 1999. Charleston
SC USA: 132.
- [68] Krock RP, Boyer C, Kiser MD. 32nd SAMPE Symposium 1987; 32:
1447-1460.

- [69] Knippenberg WF, Lersmacher B. Phillips Tech. Review 1976; 36: 93-103.
- [70] Kweeder JA, Ramesh NS, Campbell GA, Rasmussen DH. ANTEC 1991; 1398-1400.
- [71] Lever WE, Gerwels JM, Holland CW. Atomic energy commission RD report. Union Carbide Corp. 1969.
- [72] Lo WL. Journal of Cellular Plastics 1965; January: 45-50.
- [73] Oberlin A, Rouzaud JN, Goma J. Journal de Chimie Physique 1984 ; 81 : 701 -710.
- [74] Mehta R, Anderson DP, Hager JW, Thorp K. 21st Biennial Conf. on Carbon. Buffalo, NY; 1993: 102-103.
- [75] Mehta R, Anderson DP, Hager JW. Carbon 2003; 41: 2159-2179.
- [76] MER Corporation. Product literature, 2004.
- [77] Mordkovich VZ. Theo. Found. Chem. Engr. 2003; 37; 429-438.
- [78] Morgan DR. Dallas TX USA, University of North Texas, Masters Thesis, 2001.
- [79] Morgan DR, Biggers SB, Grujicic M. Engineering, Construction, and Operations in Challenging Environments. ASCE. Houston TX USA; 2004: 960-967.
- [80] Oak Ridge National Labs. Carbon Foam Page.
<http://www.ms.ornl.gov/researchgroups/CMT/FOAM/foams.htm>.
2004.
- [81] Nakaniski Y. Techno. Japan 1992; 25: 108.

- [82] Plesset MS, Zwick SA. Journal of Applied Physics 1954; 29: 493-500.
- [83] Peigney A, Laurent Ch, Flahaut E, Rousset A. Ceramics International 2000; 26: 677-683.
- [84] Pocofoam. Product literature, 2004.
- [85] Pyrograf-III. Product Literature. Applied Sciences Incorporated. 2001.
- [86] Rayleigh. Philosophical Magazine 1917; 34: 94-98.
- [87] Rogers D, Plucinski J, Stansberry P, Stiller A, Zondlo J. Proceedings, International SAMPE Symposium and Exhibition. Society of Materials and Process Engineers. , 2000; 45 (I): 293-305
- [88] Rosner DE, Epstein M. Chemical Engineering Science 1972; 27: 69-87.
- [89] Sandhu SS, Hager JW. Mat. Res. Soc. Sym. 1992; 270: 35-40.
- [90] Sands AE, Scrivner ME, Paluzelle R. Atomic energy commission RD report. Union Carbide Corp. 1970.
- [91] Sanchez-Coronado J, Chung DDL. Carbon 2003; 41: 1175-1180.
- [92] Schmitt CR, Coffey AL, Schreyer JM. Atomic Energy Commission RD. report. Union Carbide Corp. 1969.
- [93] Scriven LE. Chemical Engineering Science. 1959; 10: 1-13.
- [94] Sihn S, Roy AK. J. of Mech. And Phy. Of Solids 2004; 52: 167-191.
- [95] Sihn S, Roy AK. SAMPE Int'l Symp. Long Beach, Ca. SAMPE, 1991; 230-242.
- [96] Shafi M, Flumerfelt R. Chem. Eng. Sci. 1997; 52: 627-632.

- [97] Shi D, Lian J, Peng H, Wang LM, et al. Applied Physics Letters 2003; 83: 5301-5303.
- [98] Spralding DM, Guth RA. Adv. Mat. & Proc. 2003: 29-31.
- [99] Stiller AH, Stansberry PG, Zondlo JW. US Patent 5,888,469. 1999.
- [100] Stiller AH, Stansberry PG, Zondlo JW. US Patent 6,241,957. 2001.
- [101] Stiller AH, Stansberry PG, Zondlo JW. US Patent 6,346,226. 2002.
- [102] Stiller AH, Yocum A, Plucinski J. US Patent 6,183,854. 2001.
- [103] Street J, Fricke A, Reiss L. Ind. Eng. Chem.. Fundam. 1971; 10: 54-64.
- [104] Thostenson ET, Ren Z, Chou TW. Composites Science and Technology 2001; 61: 1899-1912.
- [105] Touchstone Research Laboratory. Cfoam Homepage. www.cfoam.com. 2003.
- [106] Udaykumar H, Mittal R, Shyy W. J. of Comp. Phy. 1999; 153: 535-574.
- [107] Upadhyay RK. Advances in Polymer Technology 1985; 5: 55-64.
- [108] Venerus D. Polymer Engineering and Science 2001; 41: 1390-1398.
- [109] Vukov AJ. J. Serb. Chem. Soc. 1990; 55: 333.
- [110] Wapner PG, Hager JW. Extended abstracts, 20th biennial conf. on carbon. Santa Barbara (California, USA): American Carbon Society, 1991; 188-195.
- [111] Warren WE, Kraynik AM. J. of App. Mech. 1988; 55: 341-345.
- [112] Warren WE, Kraynik AM. J. of App. Mech. 1997; 64: 787-794.

R002591972

- [113] Weaire D, Coughlan S, Fortes AM. Journal of Materials Processing Tech. 1995; 55: 178-185.
- [114] Withers JC, Patel JP. International SAMPE Symposium and Exhibition 2000; 45: 659-663.
- [115] White JL. ACS Symposium No. 21. 1976. Washington DC. 282.
- [116] Wright Materials Research Company. Product Data Sheet. 2004.
- [117] Yakovlev VM. Plastics 1979; 53.
- [118] Yang J, Shen Z, Hao Z. Carbon 2004; 42: 1882-1885.
- [119] Ye T, Mittal R, Udaykumar HS, Shyy W. J. Comp. Physics 1999; 156: 209-240.
- [120] Ye T. Shyy W, Chung J. J. Comp. Physics 2001; 174: 781-815.
- [121] Zimmer JE, White JL. Advances in Liquid Crystals 1982; 5:157.
- [122] Zimmer JE, White JL. Carbon 1983; 21: 323.